Scilight

Bulletin of Computational Intelligence
https://www.sciltp.com/journals/bci

Article

Seismic Reliability Analysis of Concrete Arch Dams Incorporating Different Valley Shapes: Using a Surrogate Model

Mohammad Aminrad, Majid Pouraminian * and Somayyeh Pourbakhshian *

Department of Civil Engineering, Ram.C., Islamic Azad University, Ramsar, Iran
* Correspondence: majid.pouraminian@iau.ac.ir (M.P.); somayyeh.pourbakhshian@iau.ac.ir (S.P.)

How To Cite: Aminrad, M.; Pouraminian, M.; Pourbakhshian, S. Seismic Reliability Analysis of Concrete Arch Dams Incorporating Different Valley Shapes: Using a Surrogate Model. *Bulletin of Computational Intelligence* **2026**, *2*(4), 318–343. https://doi.org/10.53941/bci.2026.100017

Received: 25 September 2026
Revised: 19 October 2026
Accepted: 27 October 2026
Published: 5 November 2026

Abstract: Concrete arch dams are widely constructed in regions featuring deep valleys and distinctive valley shapes because of their high efficiency and economical use of materials. However, the stability of these structures under earthquake loading requires accurate and comprehensive analyses. Accordingly, this study investigates the seismic reliability of these dams, focusing on the effect of different valley shapes on dam safety in terms of the reliability index (β). The research variables—including the slopes on the left and right sides of the valley, the position of the valley bottom and peak ground acceleration of earthquake have been utilized across various scenarios. In this study, a response-surface surrogate model (RSM) was used to generate explicit functions describing dam behavior, ABAQUS was used for finite element (FE) analysis of the models, and MATLAB coding was employed to implement the methods for estimating the probability of failure and the β index. In addition, the probabilistic seismic response of the dams under different valley-shape conditions was evaluated through implicit dynamic analysis using the Northridge, Friuli, and Trinidad earthquake records at different intensity levels. Examining four valley shapes (i.e., V-shaped, symmetric and asymmetric polygonal, and U-shaped) revealed that valley shape strongly affects stress distribution and seismic load-carrying capacity. Valley shape should therefore be considered a key factor in the design and seismic performance assessment of arch dams. The results also demonstrated that symmetric valleys provide the most suitable sites for arch-dam construction and identified valley-shape asymmetry as the most important factor increasing the probability of failure. Overall, this research represents an important step toward developing simulation-based and probabilistic approaches to the design of earthquake-resistant dams.

Keywords: surrogate model; probability of failure; reliability; concrete arch dams; finite element analysis; river valley shape

1. Introduction

Concrete arch dams are among the most advanced hydraulic structures because of their high efficiency in force transfer and economical use of materials. These dams are generally constructed in narrow, deep valleys with rocky walls. The distinctive geometry of these structures enables water loads to be transferred effectively toward the sides and mountainous abutments. Nevertheless, the seismic performance of arch dams, particularly in regions of high seismicity such as Iran, is subject to substantial uncertainties. These uncertainties arise not only from material properties and earthquake intensity, but also from the geometry of the valley at the construction site, which plays a pivotal role in the seismic behavior of the dam [1]. In classical arch-dam design studies, valley

Copyright: © 2026 by the authors. This is an open access article under the terms and conditions of the Creative Commons Attribution (CC BY) license (https://creativecommons.org/licenses/by/4.0/).
Publisher's Note: Scilight stays neutral with regard to jurisdictional claims in published maps and institutional affiliations.

geometry is generally represented in a simplified form (e.g., two-dimensional symmetry or triangular sections). Geological conditions, however, have shown that the stress field at the abutments and the extent of seismic-wave transmission are strongly affected by valley shape (e.g., V-shaped, U-shaped, polygonal, or asymmetric). Valley geometry can cause stress concentration, local amplification of vibrations, or even changes in the hydrodynamic-pressure distribution pattern. Recent studies (e.g., Nikkhakian et al., 2020 [2], Zhang et al., 2024 [3]) have shown that valleys with irregular shapes and discontinuous slopes can lead to nonuniform stress distributions and increased stress concentrations at particular locations in the dam and foundation. Hence, understanding these geometric effects is essential for accurately modeling the seismic behavior of the dam and identifying critical regions. Under such conditions, conventional assessments based on deterministic methods cannot accurately represent the probability of failure or unsafe structural performance [2]. In this context, the concept of seismic reliability has emerged in recent years as a tool for analyzing the probability of failure of large dams under uncertainty. This approach treats the dynamic response of the dam as a random variable and calculates the probability that the structural response will exceed allowable limits (e.g., the critical tensile stress or allowable dam-crest displacement). Despite advances in reliability methods, no systematic study is yet available that simultaneously examines the effects of different valley shapes and seismic uncertainties on the behavior of arch dams. Most models are limited to a single valley shape, whereas safety engineering requires analyzing the dam response to earthquakes under different geometric scenarios to determine the actual range of risk. In this regard, Pouraminian and Ekrannejad (2021) [4] performed a reliability analysis of a concrete arch dam under staged-construction loads and hydrostatic pressure using Monte Carlo and response-surface methods. Pouraminian et al. (2019) [5] evaluated the probabilistic safety of a concrete arch dam based on finite element modeling (FEM) and a load-and-resistance-based reliability approximation. In another study, Pouraminian et al. (2020) [6] calculated the reliability and performed a sensitivity analysis of a concrete gravity dam by considering water height and dam-body material properties as random variables. Pouraminian and Pourbakhshian (2020) [7] also performed multi-objective optimization of the geometric shape of an arch dam. Recent studies have also focused on integrating, developing, and improving analytical methods in this area. For instance, Sun et al. (2026) [8] evaluated the improved seismic performance of high asphalt-concrete-core dams based on an integrated seismic-performance index. Chen et al. (2026) [9] performed a probabilistic seismic fragility analysis of high arch dams using clustering. Xu et al. (2025) [10] investigated the seismic performance of concrete dams considering the combined effects of waves and incidence direction under near-fault ground motions. Wu et al. (2025) [11] also proposed a hybrid model based on a cloud-model mechanism for the safety assessment of high arch dams based on spatiotemporal deformation. The fundamental unresolved issue addressed in this study, however, is the substantial effect of this reliability on the valley shape and the lack of sufficient attention to this parameter in the design and assessment process. Considering the mentioned points, the present study was designed to investigate the seismic reliability of concrete arch dams considering different valley shapes. This study evaluates the effect of changes in valley geometry on the probability of dam failure using advanced numerical methods such as three-dimensional FEM and Monte Carlo Simulation (MCS), together with other non-sampling methods, including the First-Order Reliability Method (FORM) and the Second-Order Reliability Method (SORM). The relationship between the probability of failure (P_f) and the reliability index (β) is defined by the inverse standard normal cumulative distribution function, as given in Equation (1).

$$P_f = \Phi\left(\frac{0-\mu_g}{\sigma_g}\right) = \Phi(-\beta) \tag{1}$$

Where, the standard normal cumulative distribution function Φ is expressed by Equation (2), in which μ and σ respectively denote the mean and standard deviation of the Limit-State Function (LSF), represented by g.

$$\Phi(x) = \frac{1}{\sigma_g\sqrt{2\pi}} exp\left[-\frac{1}{2}\left(\frac{g-\mu_g}{\sigma_g}\right)^2\right] \tag{2}$$

FORM was proposed by Hasofer and Lind in 1974 [12]. In this method, the Design Point (DP) in the transformed standardized coordinate system is used to calculate the reliability index. In FORM, the curved failure region is estimated after calculating the shortest distance from the coordinate origin to the limit-state function (which is the reliability index, or β) by means of a linearizing transformation (Figure 1), and the function is the inverse standard normal cumulative distribution function. To improve the performance of FORM for nonlinear limit-state functions, Fiessler et al. (1979) [13] established SORM and used a second-order approximation to calculate the probability of failure based on the reliability index (Figure 2). Metropolis and Ulam in 1949 introduced MCS as one of the most fundamental and widely used methods for estimating structural failure

probability [14]. The MCS, which covers the entire sample space with the generated samples, is regarded as the most accurate method in this field (Figure 3).

Concrete dams are considered part of a nation's critical infrastructure; their failure would result in irreparable damage. Consequently, a higher safety margin is incorporated into the design of such dams. One metric used to establish minimum safety standards—based on probabilistic calculations—is known as the target reliability index (β^{Target}). This index has been recommended by Pouraminian et al. [5] to fall within the range of 4.2 to 4.6 for important infrastructures and concrete arch dams.

Overall, the principal issue in the present study is that the simultaneous effects of valley shape and seismic uncertainties have not yet been comprehensively investigated in the seismic design and assessment of arch dams. This scientific gap may limit existing assessments of ultimate safety or lead to over-optimistic results. Addressing this deficiency is the central objective of the present proposed study. The results may contribute to more accurate geometric design, selection of a suitable dam-construction site, and determination of realistic seismic safety factors for existing and new dams.

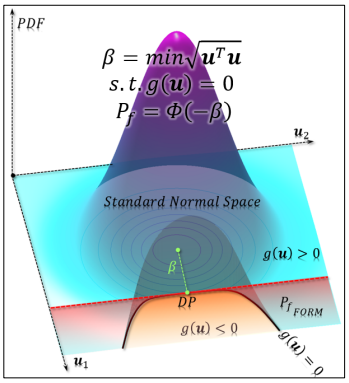


Figure 1. FORM.

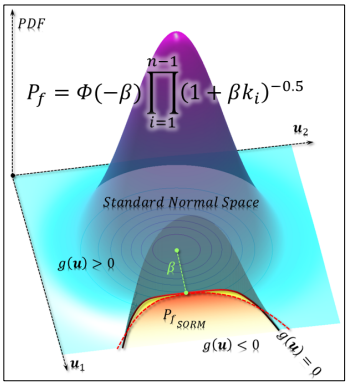


Figure 2. SORM.

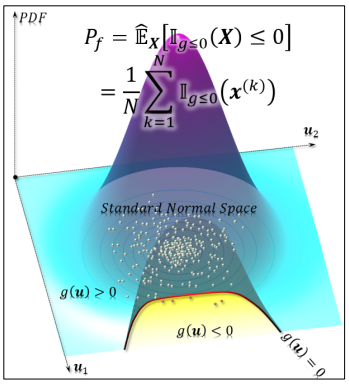


Figure 3. Monte Carlo method.

The remainder of this article introduces the Karun-4 arch dam as the reference model, presents validation of the finite element model, and develops and solves the seismic-reliability problem for the dam. Finally, an overall conclusion and recommendations for future studies are presented.

2. Karun-4 Arch Dam

A suitable case-study option for this section is Karun-4 Dam, known as the tallest arch dam in Iran. A view of this dam is shown in Figure 4.



Figure 4. Karun-4 concrete arch dam.

The dam is located in an area of very high seismic hazard. Information and data for this dam, including the geometry of the dam body and the type and mechanical properties of its constituent materials, are provided in the following lines [15]. The 230-m-high Karun-4 double-curvature concrete arch dam, the tallest dam in Iran, is located on the Karun River upstream of the confluence of the Karun and Monj rivers, 180 km southwest of Shahrekord in Chaharmahal and Bakhtiari Province. The dam-crest elevation is 1032 m above mean sea level, the total height of the dam body is 270 m, and its height above the foundation is 190 m. The crest is 7 m wide, the base is 37 m wide, and the crest length is 440 m. The two-dimensional section and three-dimensional form of the dam are presented in Figure 5 and Figure 6, respectively. The total reservoir volume is 2.3 billion m^3, and the volume of concrete placed in dam construction is 1.8 million m^3 [15,16].

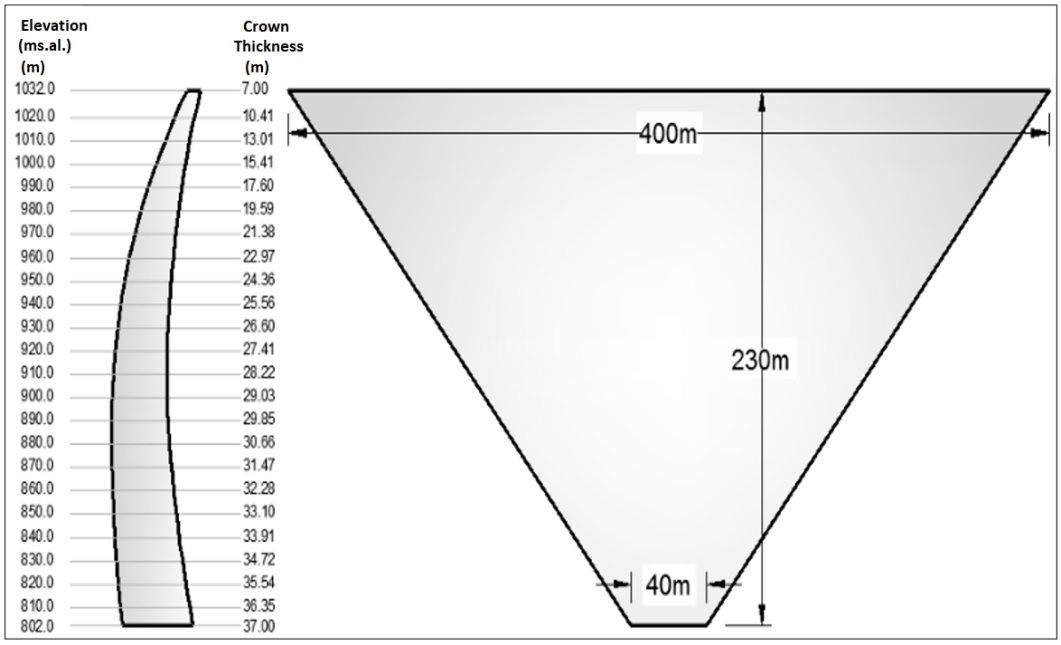


Figure 5. Two-dimensional section of Karun-4 Dam.

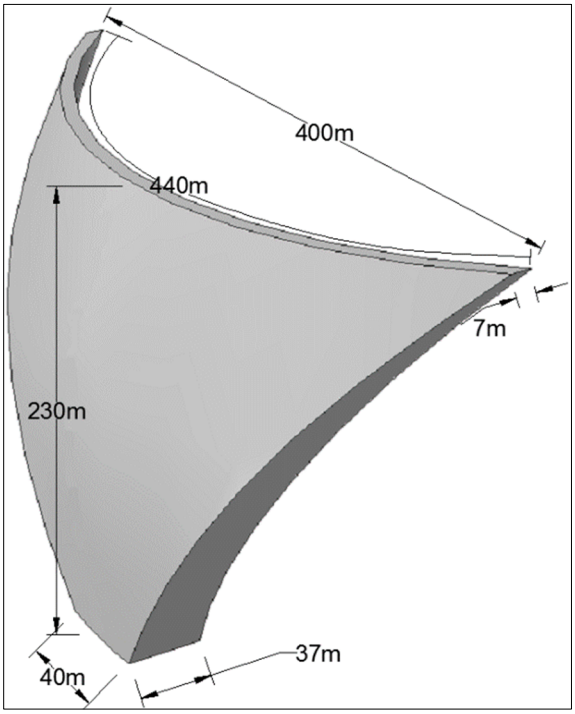


Figure 6. Three-dimensional section of Karun-4 Dam.

3. Validation of the Finite Element Model

The analytical results reported in [15] were used to evaluate the accuracy of the modeling. After designing the Karun-4 double-curvature concrete arch dam, the company applied ANSYS to perform a dynamic analysis of the dam body by the peak ground acceleration (PGA) method for a PGA of 0.15 g under the Northridge earthquake. The obtained results of that analysis were used in the present study to assess modeling accuracy. Based on the information obtained from [15], the exact dam geometry and material properties were again simulated and analyzed in ABAQUS. Linear elastic concrete properties were used for the dam-body model: a concrete unit weight of 2400 kg/m^3 and, for concrete with a compressive strength of 30 MPa, an elastic modulus of 28 GPa and a Poisson's ratio of 0.3. The records of Kobe, Friuli, and Trinidad earthquakes, which occurred at sites with characteristics similar to those of the Karun-4 Dam site, were also obtained from the PEER website. The other two earthquakes are used in the subsequent analyses. SeismoSignal was used for scaling, fitting, and effective-duration correction of the earthquake records. The duration correction was performed by removing the intervals containing the initial and final 5% of earthquake energy. Three different steps were defined for a comprehensive analysis of the dam body: (a) static analysis, to define the initial boundary conditions as fixed at the dam-abutment boundaries and to apply the gravity load from the self-weight of the dam body; (b) implicit dynamic analysis (1 s), to apply hydrostatic, hydrodynamic, and uplift loads; and (c) implicit dynamic analysis (20 s), to apply the earthquake load to the support conditions (Figure 7).

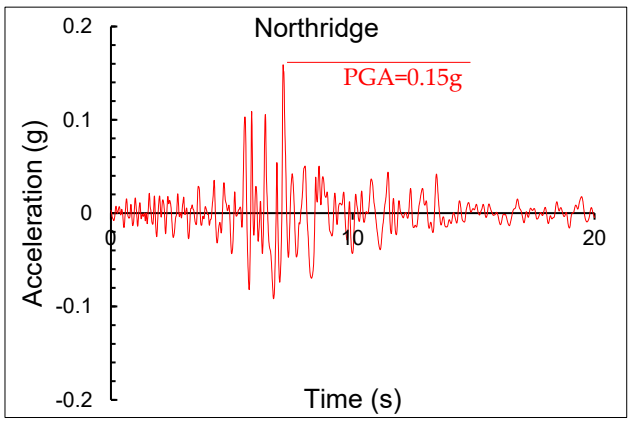


Figure 7. Corrected acceleration record of the Northridge earthquake.

In accordance with the USBR code [17], this record is also applied in the two horizontal directions with a coefficient of g and in the vertical direction with a coefficient of 0.3 g = 0.3 × 9.81 = 2.943 m/s^2. The model was meshed using four-node continuous linear tetrahedral elements designated C3D4. A mesh-sensitivity analysis was also performed to determine the optimum mesh dimensions. Five different approximate mesh sizes, ranging from 5 m to 25 m, were considered (Figure 8).

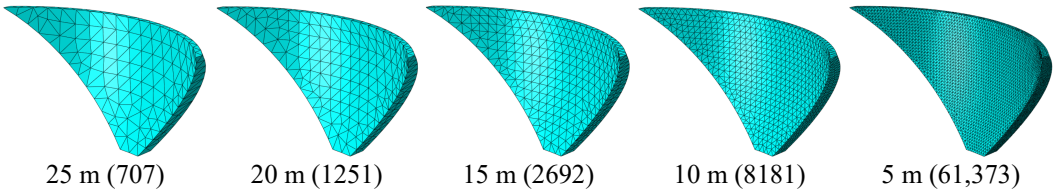


Figure 8. Mesh sizes (and numbers of elements) in the mesh-sensitivity analysis.

In each case, the maximum stress in the dam body was used as the comparison criterion. Figure 9 shows that an approximate mesh size of 25 m resulted in a stress of 2.78 MPa in the dam body. Stress changed substantially with element size until reducing the mesh size from 10 m to 5 m no longer affected the response. The maximum stress changed by only 0.43%, which is negligible, and converged to 4.61 MPa. An approximate mesh size of 10 m was therefore used for the dam body in the remainder of the study. Accordingly, after modeling in ABAQUS and performing the dynamic analysis, the displacements developed at the dam crest were used as the validation criterion, and the ANSYS results from [15] were compared with those of the model developed in the present article. The responses obtained from the two programs were approximately equal, and the peaks and troughs of the plots were in good agreement. The difference between the maximum plotted values was 1.4%, confirming the accuracy of the modeling (Figure 10).

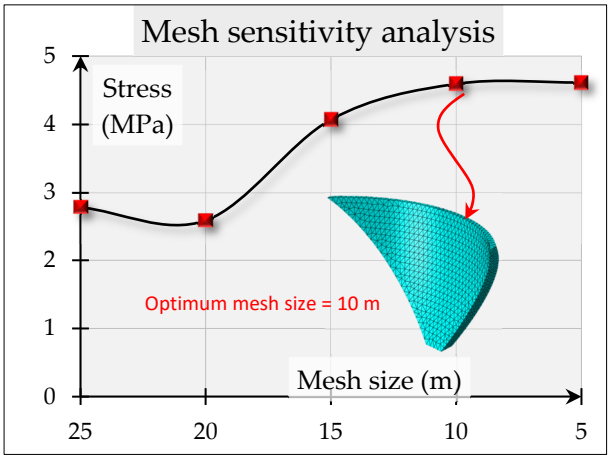


Figure 9. Variation in maximum stress with element size.

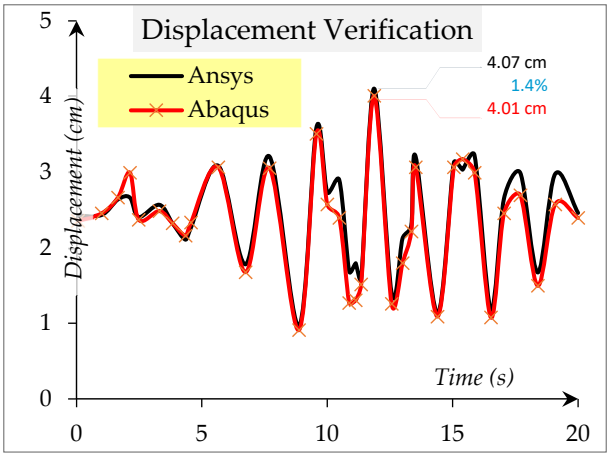


Figure 10. Comparison of the displacements developed at the dam crest.

4. Experimental Design, Sample Analysis, and Derivation of Response-Surface Relationships

Response Surface Methodology (RSM) was used in this research to develop explicit functions representing the structural response of the concrete arch dam as the input parameters vary. The method designs the experimental matrix based on the number of variables and the specified upper and lower bounds of each variable. The number of tests and the level of each variable in each test are determined accordingly. When the number of variables is large, this method is preferable to computationally intensive methods such as full factorial design. The experimental design is such that statistically reliable results can be obtained even without test replication. The method therefore facilitates the research process and reduces time and cost [18]. Central Composite Design (CCD), Box-Behnken, and Doehlert are the three principal response-surface design methods. Among these methods, CCD is more reliable [19] and then it was used in this study. In RSM, logical upper and lower bounds are first defined for the variables. The interval between the bounds is then divided into equal values according to the required accuracy of the functions and mapped to the corresponding values from −α to +α [18]. Figure 11 presents the models at different levels for a two-dimensional problem.

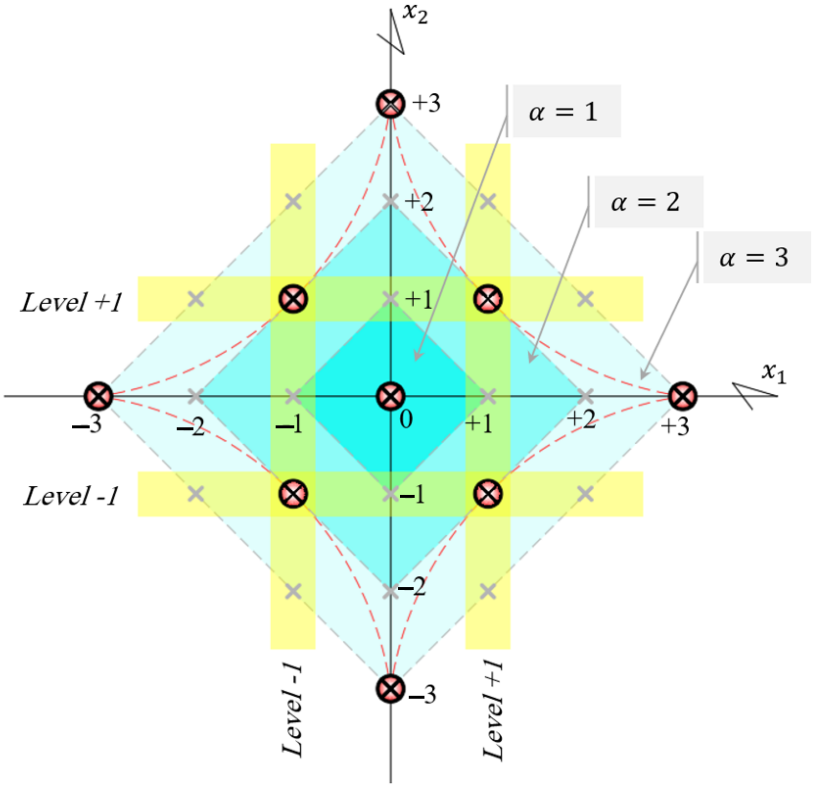


Figure 11. Description of the different levels in the response surface.

The upper and lower bounds of the variable were calculated with α and the corresponding values of +1 and −1 available for a parameter. This calculation is performed automatically in Design-Expert, and it is only necessary to define the required level as α and the corresponding +1 and −1 values for each parameter. Explicit relationships describing system performance were established by developing the model design from the validated model using Design Expert version 7.0.0. The models were subjected to finite element analysis in ABAQUS 2024, and the reliability calculations were performed using MATLAB R2015a code. As noted, four different valley-shape scenarios were considered: V-shaped, symmetric polygonal, asymmetric polygonal, and symmetric U-shaped valleys. The variables for each valley shape are presented in Figure 12a to Figure 12d. The last variable in each scenario is the applied earthquake acceleration. As noted in the validation section, the Northridge, Friuli, and Trinidad earthquakes were used for the analysis. After the earthquake durations were corrected to 20 s, the PGA was also treated as a variable from 0.05g to 0.35g (Figure 13).

The models proposed by the response surface in each scenario and the analyses related to each case are presented below in four separate subsections. Each subsection includes: (a) valley geometry and the corresponding variables; (b) mapped variable values; (c) response-surface models and analytical results; (d) finite element model form and stress contour; (e) the relationship provided by the response surface; and (g) the limit-state-function

relationship. The results of the reliability analysis against the acceleration records of the three different earthquakes are also presented separately for all four scenarios in the following section.

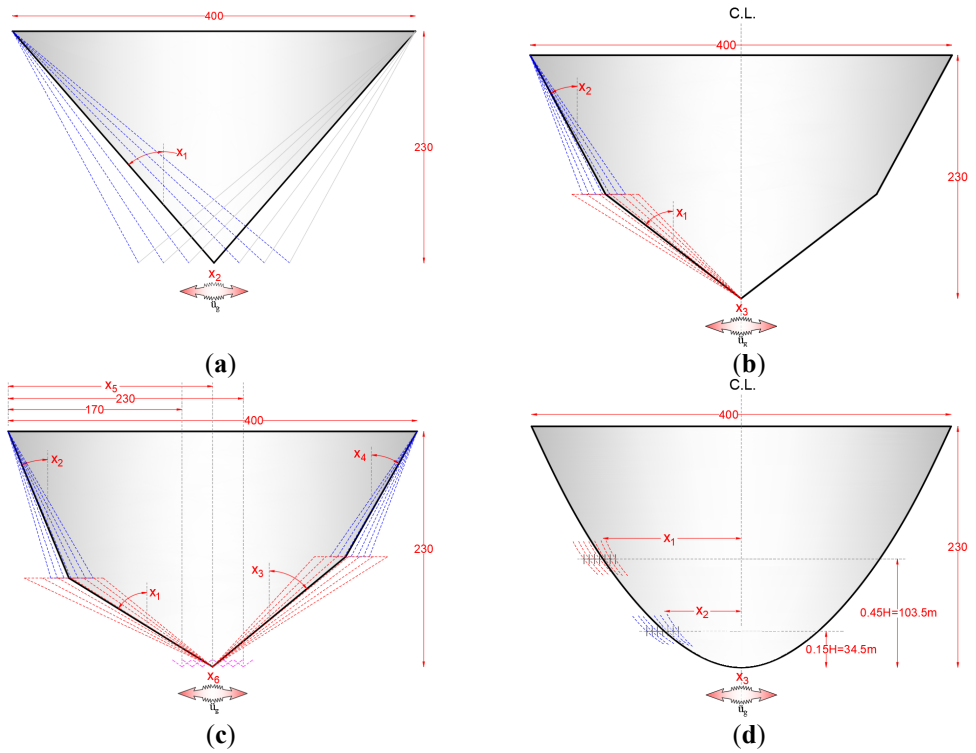


Figure 12. Different valley-shape scenarios considered in the present study. (**a**) V-shaped valley; (**b**) Symmetric polygonal valley; (**c**) Asymmetric polygonal valley; (**d**) U-shaped valley.

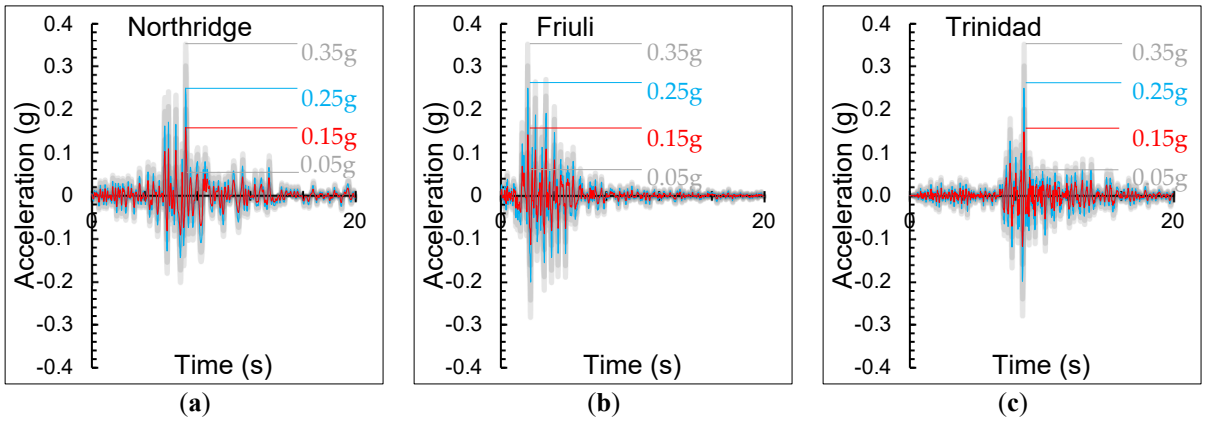


Figure 13. Variable peak-amplitude spectra of the earthquake records. (**a**) Northridge earthquake; (**b**) Friuli earthquake; (**c**) Trinidad earthquake.

4.1. Scenario I: Asymmetric V-Shaped Valley

The dam height (230 m) and the valley width at the dam crest (400 m) were considered constant in all analyses and set equal to those of Karun-4 Dam. In this scenario, the valley was assumed to be V-shaped. The abutment angle relative to the vertical line, denoted by x_1 in Figure 14, was varied from 30° to 48°. In all models, the earthquake acceleration record was applied at the site where the dam body meets the abutments. In this scenario, the acceleration record was denoted by x_2, and PGA varied from 0.05 g to 0.35 g. The analysis was repeated for the three earthquakes under consideration.

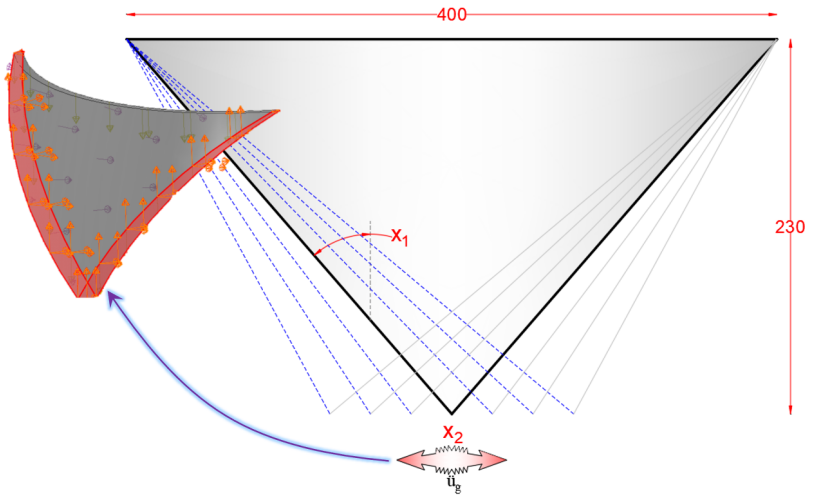


Figure 14. Valley geometry and the first and second variables in the first scenario.

The mapping of the variables to the range from −3 to +3 is also shown in Table 1. Using this procedure, 13 models were generated through RSM. These models were simulated and analyzed separately in ABAQUS. The first column of Table 2 gives the model numbers, while the second and third columns give the variable values proposed by the response surface. The remaining columns present the results of the ABAQUS analyses of these models. The results were obtained from the maximum values of the stress and displacement contours and were analyzed and reported separately for the three earthquakes. Table 3 shows the numerical values of the model parameters, the two-dimensional valley shape, the three-dimensional form developed in ABAQUS together with the boundary conditions, and the stress contours for selected models.

Table 1. Mapping of the first-scenario variables to alpha from −3 to +3.

$\alpha \rightarrow$	−3	−2	−1	0	+1	+2	+3
$x_1(°)$	30	33	36	39	42	45	48
$x_2\left(\times\frac{g}{100}\right)$	5	10	15	20	25	30	35

Table 2. Response-surface models and finite element results for the first scenario.

Scenario 1								
Model	x_1 (°)	$x_2\left(\times\frac{g}{100}\right)$	Northridge (N)		Friuli (F)		Trinidad (T)	
			D (m)	S (MPa)	D (m)	S (MPa)	D (m)	S (MPa)
1	36	25	0.58	16.09	0.56	18.79	0.76	23.52
2	48	20	0.39	25.06	0.33	29.93	0.35	6.88
3	39	5	0.14	7.75	0.08	6.34	0.12	8.05
4	39	20	0.48	23.02	0.37	18.46	0.58	27.04
5	30	20	0.32	10.18	0.46	13.35	0.24	19.41
6	39	20	0.48	23.02	0.37	18.46	0.58	27.04
7	39	35	0.63	26.60	0.53	29.31	0.66	24.65
8	36	15	0.33	20.17	0.25	13.67	0.32	12.10
9	39	20	0.48	23.02	0.37	18.46	0.58	27.04
10	39	20	0.48	23.02	0.37	18.46	0.58	27.04
11	42	15	0.39	24.26	0.28	12.09	0.37	21.87
12	42	25	0.67	20.57	0.25	13.98	0.45	6.75
13	39	20	0.48	23.02	0.37	18.46	0.58	27.04

Table 3. Form, model, and stress contours of selected first-scenario models.

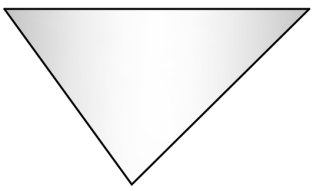
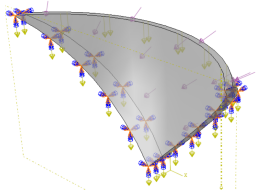
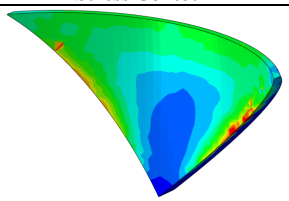
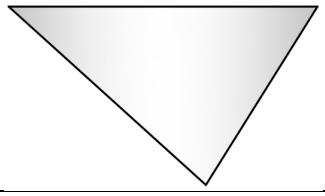
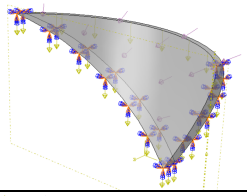
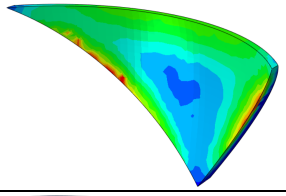
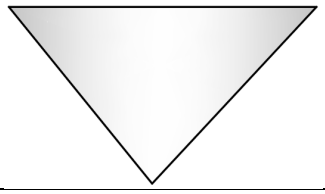
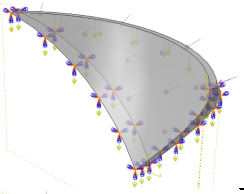
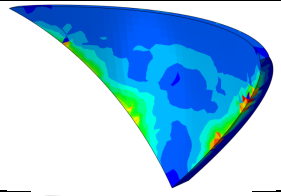
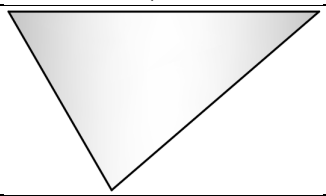
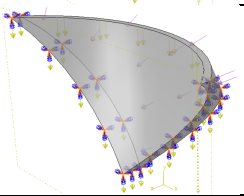
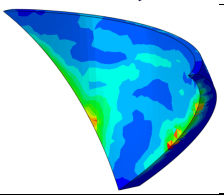
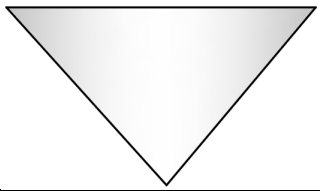
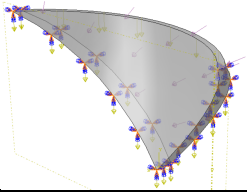
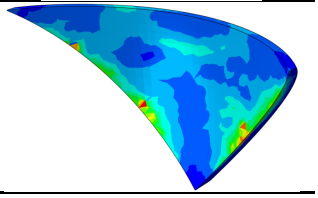
Models Property	Valley Shape	3D FE Model B.C.	Stress Contour
Model 1: $x_1 = 36$, $x_2 = 25$			

Table 3. *Cont.*

Models Property	Valley Shape	3D FE Model B.C.	Stress Contour
Model 2: $x_1 = 48$, $x_2 = 20$			
Model 3: $x_1 = 39$, $x_2 = 5$			
Model 5: $x_1 = 30$, $x_2 = 20$			
Model 11: $x_1 = 42$, $x_2 = 15$			

Accordingly, explicit mathematical relationships between the valley-slope variable (x_1) and peak earthquake acceleration (x_2), the displacement (D), and stress (S) were derived by the RSM for each case and are presented in Equations 3 to 8. The subscripts assigned to displacement and stress represent the scenario number and the initial letter of the corresponding earthquake record. For example, D_{1T} denotes the displacement developed in the first scenario under the Trinidad earthquake.

$$D_{1N}(x_1, x_2) = -2.40 + 0.12x_1 + 0.01x_2 \tag{3}$$

$$S_{1N}(x_1, x_2) = -116.58 + 5.49x_1 + 1.15x_2 - 0.06{x_1}^2 - 0.02{x_2}^2 \tag{4}$$

$$D_{1F}(x_1, x_2) = -3.44 + 0.07x_1 + 0.24x_2 \tag{5}$$

$$S_{1F}(x_1, x_2) = 2314.50 - 97.31x_1 - 158.08x_2 + 5.87x_1x_2 + 0.97{x_1}^2 + 2.26{x_2}^2 - 0.04{x_1}^2x_2 - 0.05x_1{x_2}^2 \tag{6}$$

$$D_{1T}(x_1, x_2) = -9.96 + 0.38x_1 + 0.28x_2 \tag{7}$$

$$S_{1T}(x_1, x_2) = -539.05 + 19.47x_1 + 19.18x_2 - 0.44x_1x_2 - 0.14{x_1}^2 - 0.03{x_2}^2 \tag{8}$$

In the following, symmetric polygonal valleys are evaluated using the same procedure, and their performance function is derived.

4.2. Scenario II: Asymmetric V-Shaped Valley

A different valley shape is examined in this scenario (Figure 15). By adding another slope to the valley shape, two variables, x_1 (from $45°$ to $57°$ relative to the vertical line) and x_2 (from $20°$ to $32°$ relative to the vertical line), affect the valley geometry. The earthquake force was also treated as the third random variable (x_3) ranging from $0.05g$ to $0.35g$. Table 4 shows the mapping of the variables to values from $\alpha = -3$ to $\alpha = +3$ and their division into equal intervals. Accordingly, 20 models based on three variables were proposed by the RSM. Each model was simulated separately in ABAQUS, and the resulting maximum crest displacement and maximum stress were extracted and entered in Table 5. This process was performed separately for each of the Northridge, Friuli, and Trinidad earthquakes.

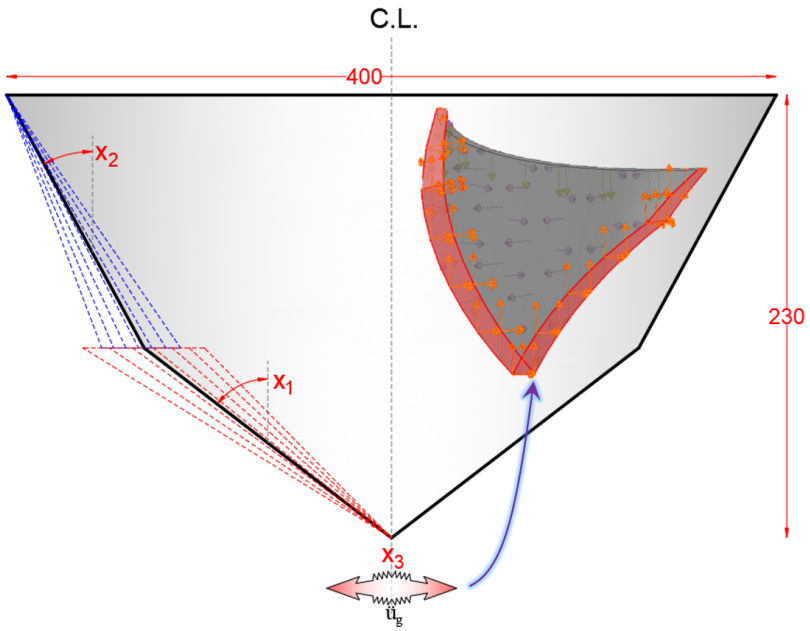


Figure 15. Valley geometry and the first through third variables in the second scenario.

Table 4. Mapping of the second-scenario variables to alpha from −3 to +3.

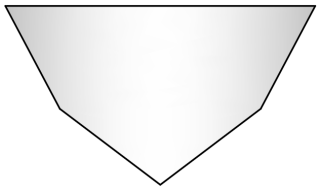
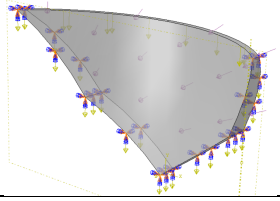
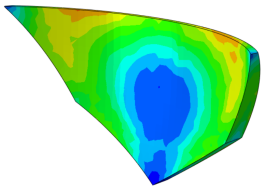
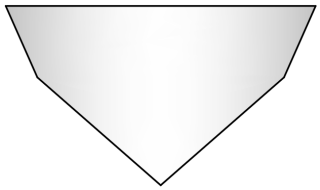
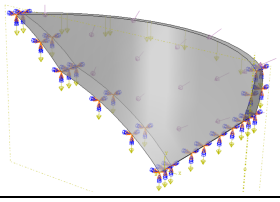
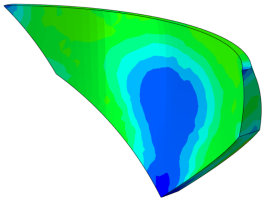
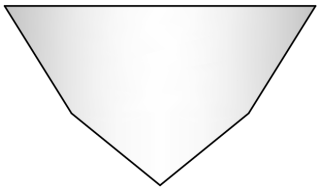
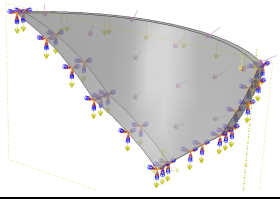
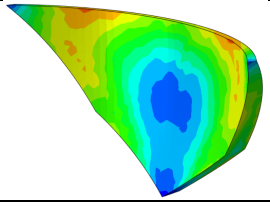
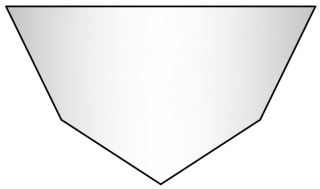
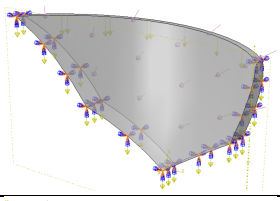
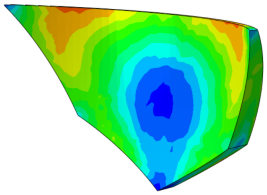
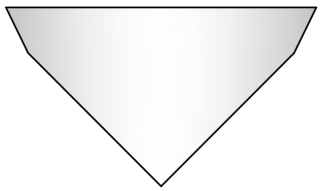
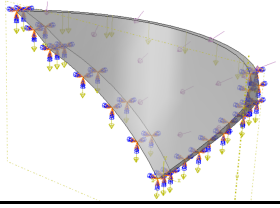
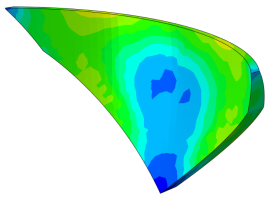
$\alpha \rightarrow$	−3	−2	−1	0	+1	+2	+3
$x_1(°)$	45	47	49	51	53	55	57
$x_2(°)$	20	22	24	26	28	30	32
$x_3\left(\times\frac{g}{100}\right)$	5	10	15	20	25	30	35

Table 5. Response-surface models and finite element results for the second scenario.

Scenario 2									
Model	x_1 (°)	x_2 (°)	$x_3\left(\times\frac{g}{100}\right)$	Northridge		Friuli		Trinidad	
				D (m)	S (MPa)	D (m)	S (MPa)	D (m)	S (MPa)
1	51	26	20	0.46	17.96	0.41	14.33	0.10	12.87
2	51	26	5	0.52	14.48	0.39	13.61	0.11	15.53
3	53	28	15	1.35	23.43	0.62	45.40	0.48	23.09
4	49	24	25	0.6	19.55	0.44	41.86	0.61	47.04
5	49	24	15	0.48	20.69	0.37	19.74	0.33	26.57
6	51	26	20	0.46	17.96	0.41	14.33	0.10	12.87
7	51	26	20	0.46	17.96	0.41	14.33	0.10	12.87
8	53	24	25	0.28	16.37	0.05	17.32	0.10	14.17
9	51	20	20	0.29	15.52	0.45	19.51	0.36	33.43
10	51	26	20	0.46	17.96	0.41	14.33	0.10	12.87
11	49	28	15	0.17	21.14	0.21	5.40	0.14	12.20
12	51	32	20	0.67	20.54	0.64	30.18	0.30	3.11
13	51	26	35	0.33	21.81	0.43	7.04	0.13	29.83
14	51	26	20	0.46	17.96	0.41	14.33	0.10	12.87
15	57	26	20	0.54	15.45	0.23	0.14	0.16	15.19
16	53	28	25	0.43	16.07	0.32	34.63	0.17	27.39
17	53	24	15	0.15	9.91	0.03	19.64	0.35	13.32
18	49	28	25	0.33	11.39	0.25	4.53	0.33	7.41
19	45	26	20	0.17	15.87	0.51	12.60	0.31	21.56
20	51	26	20	0.46	17.96	0.41	14.33	0.10	12.87

The model specifications, valley shape, three-dimensional form simulated in ABAQUS, and stress contours for five of the analyzed models are shown in Table 6.

Table 6. Form, model, and stress contours of selected second-scenario models.

Models Property	Valley Shape	3D FE Model B.C.	Stress Contour
Model 3: $x_1 = 53$, $x_2 = 28$, $x_3 = 15$			
Model 4: $x_1 = 49$, $x_2 = 24$, $x_3 = 25$			
Model 12: $x_1 = 51$, $x_2 = 32$, $x_3 = 20$			
Model 15: $x_1 = 57$, $x_2 = 26$, $x_3 = 20$			
Model 19: $x_1 = 45$, $x_2 = 26$, $x_3 = 20$			

The explicit mathematical relationships are subsequently presented as second-order polynomials incorporating variable interactions in Equations 9 to 14. It is of note that these relationships were developed separately for the independent response variables of displacement (D) and stress (S) under the Northridge, Friuli, and Trinidad earthquakes, denoted by the subscripts N, F, and T, respectively. The subscript 2 in each formula denotes the second scenario.

$$D_{2N}(x_1, x_2, x_3) = 49.83 - 0.95x_1 - 2.80x_2 + c + 0.06x_1x_2 - 0.01x_1x_3 - 0.01x_2x_3 \quad (9)$$

$$S_{2N}(x_1, x_2, x_3) = 708.12 - 13.44x_1 - 27.60x_2 + 0.94x_3 + 0.65x_1x_2 + 0.12x_1x_3 - 0.28x_2x_3 - 0.06{x_1}^2 \quad (10)$$

$$D_{2F}(x_1, x_2, x_3) = 45.81 - 0.86x_1 - 2.05x_2 + 0.36x_3 + 0.03x_1x_2 \quad (11)$$

$$S_{2F}(x_1, x_2, x_3) = 2823.70 - 43.12x_1 - 156.56x_2 + 32.02x_3 + 2.96x_1x_2 - 0.42x_1x_3 - 0.39x_2x_3 - 0.24{x_1}^2 + 0.26{x_2}^2 \quad (12)$$

$$D_{2T}(x_1, x_2, x_3) = 24.87 - 0.56x_1 - 1.30x_2 + 0.70x_3 + 0.02x_1x_2 - 0.01x_1x_3 \quad (13)$$

$$S_{2T}(x_1, x_2, x_3) = 3384.20 - 71.67x_1 - 125.09x_2 + 12.83x_3 + 2.40x_1x_2 - 0.13x_1x_3 - 0.27x_2x_3 + 0.10{x_1}^2 + 0.10{x_2}^2 + 0.03{x_3}^2 \quad (14)$$

4.3. Scenario III: Asymmetric Polygonal Valley

The present scenario was obtained by adding three variables to the previous scenario. As shown in Figure 16, the angles x_1 and x_2 relative to the vertical line correspond to the slopes on the left side of the valley, while the angles x_3 and x_4 relative to the vertical line correspond to the slopes on the right side. The variable x_5 presents the position of the valley bottom, and x_6, the final variable as in the previous cases, shows the PGA. As shown in the figure, this acceleration is applied to the lower part of the dam body where it contacts the abutment. In Table 7, the variables were mapped to the range from −3 to +3 at equal intervals. The angles x_1 and x_3 ranged from 45° to 57°, the angles x_2 and x_4 from 20° to 32°, the valley-bottom position (x_5) from 170 m to 230 m (measured from the left corner of the valley), and the PGA from 5% to 35%.

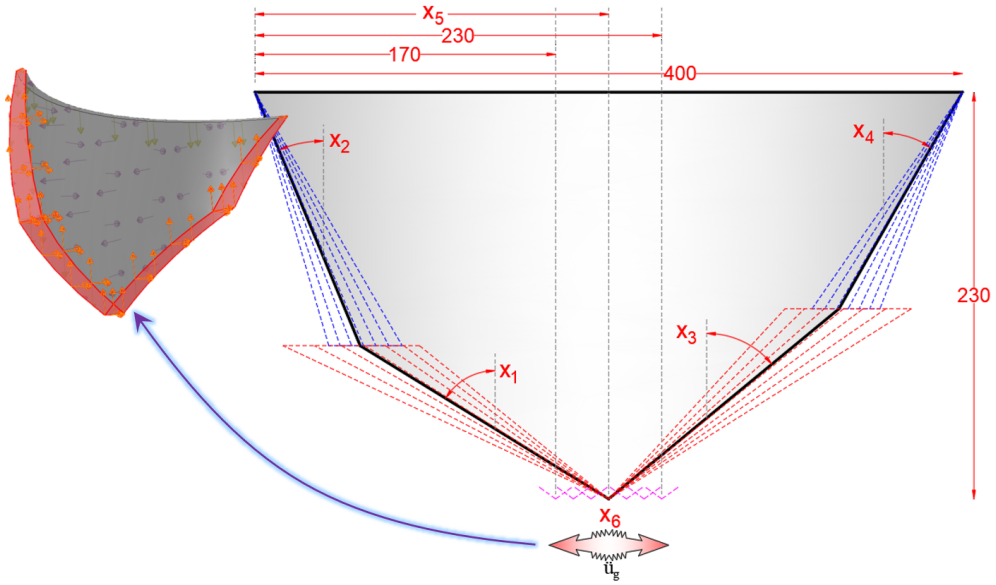


Figure 16. Valley geometry and the first through sixth variables in the third scenario.

Table 7. Mapping of the third -scenario variables to alpha from −3 to +3.

$\alpha \rightarrow$	−3	−2	−1	0	+1	+2	+3
$x_1(°)$	45	47	49	51	53	55	57
$x_2(°)$	20	22	24	26	28	30	32
$x_3(°)$	45	47	49	51	53	55	57
$x_4(°)$	20	22	24	26	28	30	32
$x_5(m)$	170	180	190	200	210	220	230
$x_6\left(\times\frac{g}{100}\right)$	5	10	15	20	25	30	35

Accordingly, 86 models with different variable values were proposed by RSM (Table 8). Likewise, the first column gives the model number, columns two through seven give the variable values, and the remaining columns present the results, including crest displacement and maximum stress obtained from the ABAQUS analyses under the three different earthquake records.

Table 8. Response-surface models and finite element results for the third scenario.

Scenario 3												
Model	x_1 (°)	x_2 (°)	x_3 (°)	x_4 (°)	x_5 (m)	$x_3\left(\times\frac{g}{100}\right)$	**Northridge**		**Friuli**		**Trinidad**	
							D (m)	**S (MPa)**	**D (m)**	**S (MPa)**	**D (m)**	**S (MPa)**
1	51	26	51	26	200	20	0.35	9.34	0.39	11.47	0.36	8.65
2	53	24	49	28	190	25	0.16	5.15	0.15	17.61	0.25	13.10
3	49	24	53	24	190	15	0.22	7.08	0.15	4.51	0.56	5.30
4	57	26	51	26	200	20	0.28	4.83	0.25	14.91	0.77	16.82
5	53	28	49	28	190	15	0.32	2.26	0.47	2.34	0.22	0.49
6	49	28	53	28	210	25	0.39	8.79	0.53	5.51	0.47	13.32
7	51	26	51	26	200	20	0.35	9.34	0.39	11.47	0.36	8.65
8	49	24	53	28	210	15	0.09	1.06	0.14	12.93	0.36	6.01
9	53	24	49	24	210	15	0.24	5.10	0.14	11.05	0.01	7.18
10	53	24	53	24	210	25	0.38	8.70	0.40	17.43	0.83	12.07
11	51	26	51	20	200	20	0.38	14.27	0.32	17.31	0.11	11.08

Table 8. *Cont.*

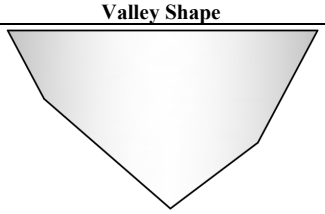
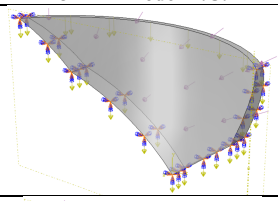
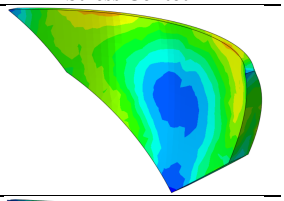
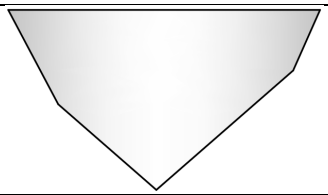
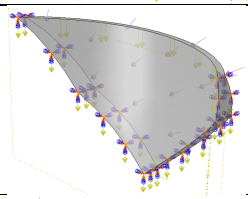
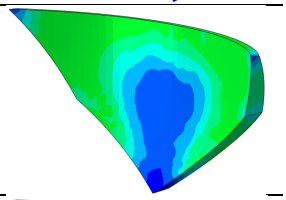
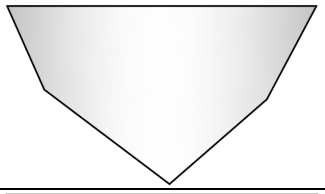
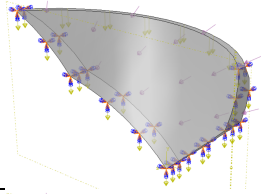
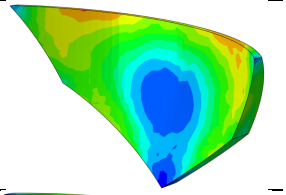
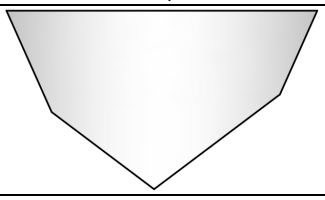
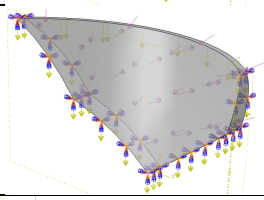
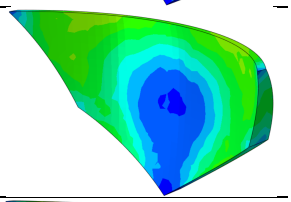
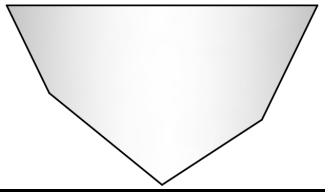
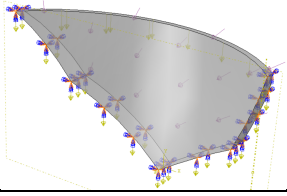
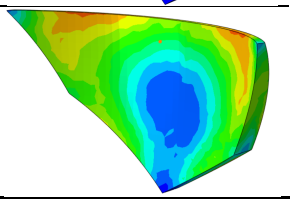
Scenario 3												
Model	x_1 (°)	x_2 (°)	x_3 (°)	x_4 (°)	x_5 (m)	$x_3\left(\times\frac{g}{100}\right)$	Northridge		Friuli		Trinidad	
							D (m)	S (MPa)	D (m)	S (MPa)	D (m)	S (MPa)
12	51	26	51	26	200	5	0.07	0.19	0.05	2.46	0.03	3.50
13	53	24	53	28	190	25	0.43	9.35	0.14	13.29	0.38	17.19
14	49	28	49	24	190	15	0.11	9.69	0.09	11.41	0.63	14.47
15	49	28	53	24	210	25	0.46	7.77	0.32	15.57	0.25	18.38
16	53	24	49	24	190	25	0.17	2.99	0.71	14.80	0.19	9.43
17	53	28	53	24	210	25	0.30	10.50	0.32	15.57	0.38	2.46
18	53	24	49	24	210	25	0.12	12.73	0.45	12.29	0.44	10.09
19	53	24	53	28	210	25	0.56	14.73	0.31	23.39	0.50	12.46
20	53	24	53	24	190	15	0.19	7.66	0.08	10.85	0.52	4.01
21	53	28	49	28	210	15	0.36	7.10	0.17	4.41	0.21	8.72
22	49	28	53	28	190	25	0.16	11.04	0.44	0.88	0.40	16.24
23	53	24	53	28	190	15	0.08	1.95	0.32	10.89	0.42	5.40
24	53	28	53	28	190	25	0.37	9.85	0.45	8.45	0.49	1.39
25	51	26	51	26	200	35	0.82	19.11	0.67	18.22	0.81	19.05
26	49	24	49	24	190	15	0.26	7.56	0.15	12.73	0.20	2.75
27	53	28	49	24	190	25	0.10	8.28	0.46	7.59	0.97	13.66
28	49	28	49	28	190	15	0.35	1.92	0.47	14.40	0.38	10.89
29	51	26	51	26	200	20	0.35	9.34	0.39	11.47	0.36	8.65
30	51	26	51	26	200	20	0.35	9.34	0.39	11.47	0.36	8.65
31	49	24	53	28	210	25	0.10	3.56	0.68	16.89	0.63	0.38
32	53	28	49	24	190	15	0.27	2.67	0.37	8.21	0.21	4.44
33	51	26	45	26	200	20	0.04	15.03	0.47	16.93	0.44	17.67
34	49	24	53	28	190	25	0.12	11.31	0.78	10.74	0.32	15.18
35	49	28	49	28	190	25	0.05	4.94	0.81	7.98	0.56	15.95
36	51	26	51	26	230	20	0.41	14.81	0.56	11.89	0.18	3.55
37	53	28	53	24	190	15	0.23	1.34	0.40	1.41	0.34	5.73
38	53	28	49	28	210	25	0.36	3.28	0.28	11.48	0.49	15.87
39	49	28	49	24	210	25	0.26	16.33	0.20	19.74	0.32	16.52
40	49	24	49	28	190	25	0.30	17.88	0.28	9.68	0.50	7.80
41	51	26	51	26	200	20	0.35	9.34	0.39	11.47	0.36	8.65
42	49	28	49	28	210	25	0.68	11.51	0.77	6.59	0.74	2.86
43	51	32	51	26	200	20	0.32	1.99	0.19	2.71	0.47	17.51
44	53	24	53	28	210	15	0.35	5.58	0.35	11.16	0.14	14.35
45	51	26	51	26	200	20	0.35	9.34	0.39	11.47	0.36	8.65
46	53	24	49	28	210	25	0.61	3.41	0.31	4.10	0.64	25.47
47	53	24	53	24	210	15	0.32	10.25	0.50	8.36	0.28	1.96
48	51	26	51	26	200	20	0.35	9.34	0.39	11.47	0.36	8.65
49	49	28	53	24	190	15	0.34	7.28	0.16	0.08	0.21	0.48
50	49	24	49	28	190	15	0.11	9.63	0.08	9.75	0.37	9.44
51	49	28	49	24	210	15	0.36	9.54	0.12	9.11	0.12	5.44
52	51	26	51	26	200	20	0.35	9.34	0.39	11.47	0.36	8.65
53	49	28	53	28	190	15	0.02	4.02	0.21	3.86	0.13	4.16
54	49	28	49	24	190	25	0.19	13.66	0.09	22.05	0.21	14.81
55	49	28	53	24	190	25	0.29	16.88	0.30	5.59	0.24	8.27
56	49	24	53	24	190	25	0.29	12.94	0.50	4.42	0.52	13.55
57	53	24	53	24	190	25	0.34	0.09	0.11	11.77	0.22	10.97
58	49	24	53	24	210	15	0.08	7.76	0.32	4.04	0.08	11.61
59	53	24	49	28	210	15	0.25	1.12	0.12	4.79	0.13	5.97
60	49	24	49	24	190	25	0.53	7.27	0.73	15.58	0.14	5.89
61	53	28	49	24	210	15	0.12	10.78	0.14	10.58	0.13	12.90
62	49	24	53	28	190	15	0.33	7.96	0.50	3.65	0.33	4.32
63	49	24	49	24	210	25	0.40	18.98	0.41	15.67	0.39	9.81
64	49	28	49	28	210	15	0.07	8.18	0.57	5.00	0.60	15.87
65	49	28	53	28	210	15	0.34	4.28	0.02	9.67	0.08	11.63
66	53	28	53	24	190	25	0.41	1.34	0.41	11.34	0.27	16.73
67	49	24	49	28	210	15	0.28	9.08	0.58	4.17	0.43	3.82
68	51	26	51	26	170	20	0.11	2.38	0.57	4.92	0.35	9.01
69	53	28	53	28	210	25	0.13	0.97	0.14	1.90	0.15	16.67
70	51	26	51	26	200	20	0.35	9.34	0.39	11.47	0.36	8.65
71	49	24	49	24	210	15	0.17	3.67	0.11	1.00	0.49	13.46
72	53	28	49	24	210	25	0.24	8.58	0.19	20.77	0.42	13.27
73	51	26	51	32	200	20	0.11	5.52	0.13	17.22	0.13	17.36
74	53	24	49	28	190	15	0.21	2.25	0.05	8.37	0.43	0.68
75	51	20	51	26	200	20	0.42	10.93	0.69	11.78	0.57	16.59
76	51	26	57	26	200	20	0.02	7.41	0.02	1.53	0.07	14.95
77	49	24	53	24	210	25	0.55	0.04	0.66	11.18	0.68	2.88
78	53	28	53	24	210	15	0.24	5.46	0.28	6.19	0.33	2.12
79	45	26	51	26	200	20	0.44	2.83	0.38	1.86	0.64	5.36
80	53	24	49	24	190	15	0.02	0.03	0.13	11.61	0.25	1.39
81	53	28	49	28	190	25	0.48	13.93	0.57	4.89	0.36	4.63

Table 8. *Cont.*

Scenario 3												
Model	x_1 (°)	x_2 (°)	x_3 (°)	x_4 (°)	x_5 (m)	$x_3\left(\times\frac{g}{100}\right)$	**Northridge**		**Friuli**		**Trinidad**	
							D (m)	**S (MPa)**	**D (m)**	**S (MPa)**	**D (m)**	**S (MPa)**
82	51	26	51	26	200	20	0.35	9.34	0.39	11.47	0.36	8.65
83	49	28	53	24	210	15	0.35	1.95	0.55	10.80	0.12	1.86
84	53	28	53	28	190	15	0.13	0.30	0.41	0.95	0.37	1.12
85	49	24	49	28	210	25	0.06	8.40	0.11	10.44	0.20	10.64
86	53	28	53	28	210	15	0.39	5.74	0.25	0.49	0.34	0.94

The specifications of five sample models developed in ABAQUS, together with their two- and three-dimensional forms and stress contours, are shown in Table 9.

Table 9. Form, model, and stress contours of selected third-scenario models.

Models Property	Valley Shape	3D FE Model B.C.	Stress Contour
Model 6: $x_1 = 49, x_2 = 28,$ $x_3 = 53, x_4 = 28,$ $x_5 = 210, x_6 = 25$			
Model 14: $x_1 = 49, x_2 = 28,$ $x_3 = 49, x_4 = 24,$ $x_5 = 190, x_6 = 15$			
Model 46: $x_1 = 53, x_2 = 24,$ $x_3 = 49, x_4 = 28,$ $x_5 = 210, x_6 = 25$			
Model 57: $x_1 = 53, x_2 = 24,$ $x_3 = 53, x_4 = 24,$ $x_5 = 190, x_6 = 25$			
Model 76: $x_1 = 51, x_2 = 26,$ $x_3 = 57, x_4 = 26,$ $x_5 = 200, x_6 = 20$			

Equations 15 to 20 present the explicit response-surface formulas for the third scenario (3) for displacement (D) in metres and stress (S) in MPa, based on the six variables x_1 to x_6 under the three different earthquakes (N, F, and T).

$$D_{3N}(x_1, x_2, x_3, x_4, x_5, x_6) = -14.50 - 0.42x_1 + 0.06x_2 + 0.98x_3 - 0.16x_4 + 0.01x_5 - 0.01x_6 + 0.01x_1x_4 \quad (15)$$

$$S_{3N}(x_1, x_2, x_3, x_4, x_5, x_6) = 37.14 - 5.26x_1 + 12.83x_2 - 6.06x_3 + 2.74x_4 + 0.29x_5 + 4.72x_6 + 0.19x_1x_3 + 0.05x_1x_4 + 0.05x_1x_5 - 0.04x_1x_6 - 0.11x_2x_3 - 0.13x_2x_4 + 0.02x_2x_6 + 0.08x_3x_4 - 0.03x_3x_5 - 0.02x_3x_6 - 0.03x_4x_5 + 0.02x_4x_6 - 0.16{x_1}^2 - 0.09{x_2}^2 + 0.03{x_3}^2 \quad (16)$$

$$D_{3F}(x_1, x_2, x_3, x_4, x_5, x_6) = -51.23 + 0.71x_1 + 0.09x_2 + 0.67x_3 + 0.91x_4 + 0.42x_6 - 0.01x_1x_4 + 0.01x_2x_4 \quad (17)$$

$$S_{3F}(x_1, x_2, x_3, x_4, x_5, x_6) = 67.72 + 8.76x_1 + 40.12x_2 - 18.24x_3 - 3.32x_4 - 2.69x_5 - 1.33x_6 - 0.29x_1x_2 + 0.20x_1x_3 - 0.07x_1x_4 + 0.03x_1x_6 - 0.31x_2x_3 - 0.35x_2x_4 + 0.03x_2x_5 - 0.01x_2x_6 + 0.28x_3x_4 + 0.07x_3x_5 - 0.02x_4x_5 - 0.08x_4x_6 + 0.01x_5x_6 - 0.09{x_1}^2 - 0.12{x_2}^2 - 0.07{x_3}^2 + 0.14{x_4}^2 \quad (18)$$

$$D_{3T}(x_1, x_2, x_3, x_4, x_5, x_6) = -6.87 - 1.10x_1 + 0.50x_2 + 0.54x_3 + 0.86x_4 + 0.07x_5 - 0.32x_6 - 0.01x_2x_3 \quad (19)$$

$$S_{3T}(x_1, x_2, x_3, x_4, x_5, x_6) = 446.74 - 9.72x_1 + 18.16x_2 - 11.26x_3 - 14.38x_4 + 0.84x_5 - 4.48x_6 - 0.30x_1x_2 + 0.02x_1x_3 + 0.05x_1x_4 + 0.04x_1x_5 + 0.10x_1x_6 - 0.19x_2x_3 - 0.15x_2x_4 + 0.01x_2x_6 + 0.10x_3x_4 - 0.03x_3x_5 + 0.03x_3x_6 + 0.02x_4x_5 - 0.01x_5x_6 + 0.04{x_1}^2 + 0.20{x_2}^2 + 0.18{x_3}^2 + 0.13{x_4}^2 \quad (20)$$

4.4. Scenario IV: Symmetric U-Shaped Valley

In this scenario, a U-shaped valley was simulated and evaluated in accordance with the preceding procedure. Two important elevation levels in dam-body design, based on the USBR recommendation [5,20], are 0.15 H and 0.45 H above the lower part of the valley that shown in Figure 17. To treat valley shape as a variable, an initial parabolic form with a height of 230 m and an opening width of 400 m, corresponding to the valley of Karun-4 Dam, was first simulated. The half-widths of the curve at elevations 0.45 H and 0.15 H were then treated as random variables denoted by x_1 and x_2, respectively. In Table 10, the variables were mapped to the range from −3 to +3 at equal intervals.

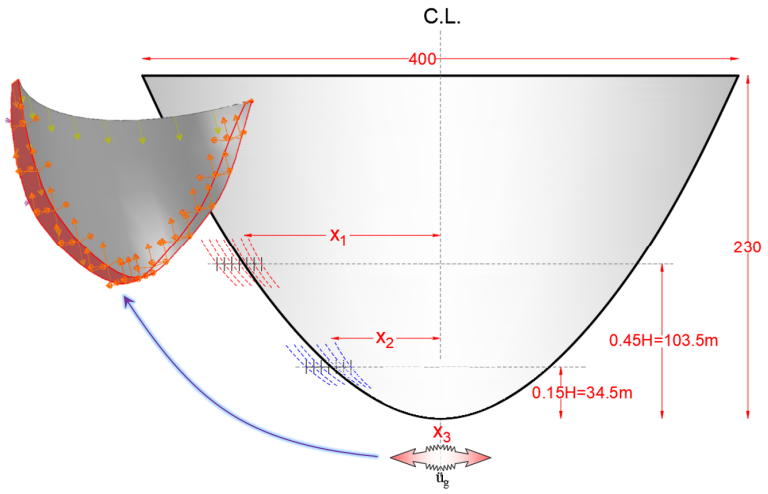


Figure 17. Valley geometry and the first through sixth variables in the fourth scenario.

Table 10. Mapping of the fourth-scenario variables to alpha from −3 to +3.

$\alpha \rightarrow$	−3	−2	−1	0	+1	+2	+3
$\boldsymbol{x_1(m)}$	120	125	130	135	140	145	150
$\boldsymbol{x_2(m)}$	60	65	70	75	80	85	90
$\boldsymbol{x_3\left(\times\frac{g}{100}\right)}$	5	10	15	20	25	30	35

Using the above geometric values as response-surface inputs, 20 different models were proposed by the response surface to generate the limit-state function, defined as exceedance of the allowable displacement and stress (Table 11). Two symmetric U-shaped valley dimensions and the earthquake-acceleration coefficient were used as the variables in this problem. Each case was simulated and analyzed in ABAQUS using the values proposed by the RSM. After finite element analysis of each model, the maximum displacement and stress were calculated

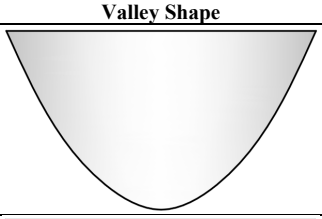
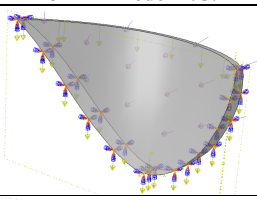
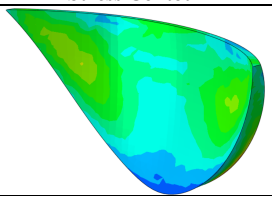
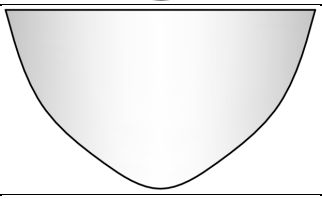
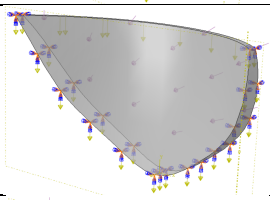
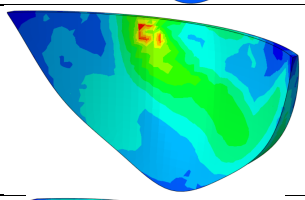
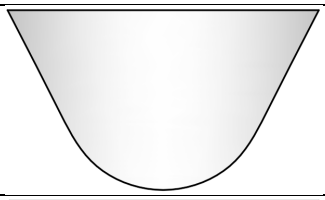
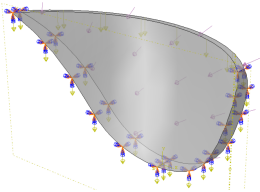
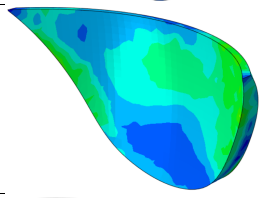
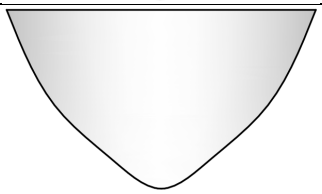
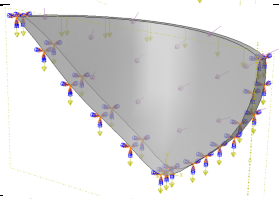
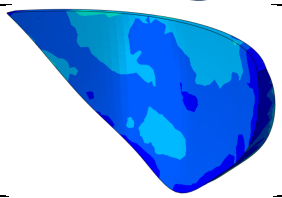
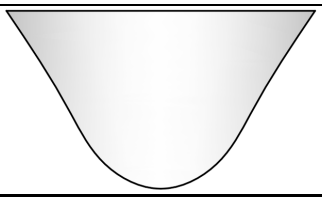
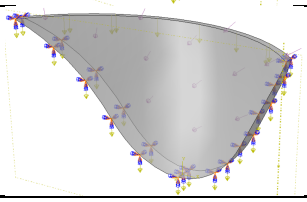
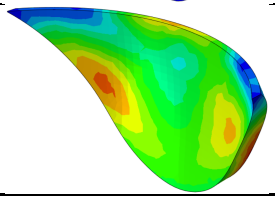
as finite element outputs. Each output was entered in the corresponding row, followed by deriving the maximum-displacement and maximum-stress functions from the RSM.

Table 11. Response-surface models and finite element results for the fourth scenario.

Model	$x_1\ (m)$	$x_2\ (m)$	$x_3\left(\times\frac{g}{100}\right)$	Scenario 4					
				Northridge		Friuli		Trinidad	
				D (m)	S (MPa)	D (m)	S (MPa)	D (m)	S (MPa)
1	135	75	20	0.32	16.03	0.40	14.74	0.49	13.98
2	130	70	25	0.33	27.21	0.42	21.58	0.36	16.32
3	135	75	35	0.76	24.87	0.61	22.46	0.72	19.06
4	140	80	25	0.37	19.60	0.37	13.46	0.42	16.41
5	135	75	20	0.32	16.03	0.40	14.74	0.46	13.98
6	150	75	20	0.34	14.57	0.39	11.19	0.35	19.92
7	130	80	25	0.47	16.77	0.58	12.70	0.53	18.69
8	130	80	15	0.48	14.62	0.28	13.50	0.41	13.77
9	135	90	20	0.35	11.04	0.37	12.81	0.32	16.28
10	135	75	20	0.32	16.03	0.40	14.74	0.46	13.98
11	135	75	20	0.32	16.03	0.40	14.74	0.46	13.98
12	135	60	20	0.31	11.97	0.43	19.24	0.31	16.70
13	140	80	15	0.43	14.00	0.38	12.43	0.30	18.91
14	140	70	25	0.47	14.01	0.41	16.27	0.46	15.63
15	140	70	15	0.58	7.06	0.65	10.17	0.62	12.02
16	120	75	20	0.47	18.41	0.42	19.00	0.31	17.53
17	130	70	15	0.30	15.53	0.37	14.55	0.23	16.07
18	135	75	20	0.32	16.03	0.40	14.74	0.46	13.98
19	135	75	20	0.32	16.03	0.40	14.74	0.46	13.98
20	135	75	5	0.16	9.63	0.15	9.53	0.17	9.21

Five models developed in ABAQUS, together with their stress contours, are presented in Table 12. An important observation from the stress contours is that stress concentration occurs at several locations in the dam body in Models 6 and 16. The increased complexity of the valley form appears to cause this stress concentration.

Table 12. Form, model, and stress contours of selected fourth -scenario models.

Models Property	Valley Shape	3D FE Model B.C.	Stress Contour
Model 1: $x_1 = 135$, $x_2 = 75$, $x_3 = 20$			
Model 6: $x_1 = 150$, $x_2 = 75$, $x_3 = 20$			
Model 9: $x_1 = 135$, $x_2 = 90$, $x_3 = 20$			
Model 12: $x_1 = 135$, $x_2 = 60$, $x_3 = 20$			
Model 16: $x_1 = 120$, $x_2 = 75$, $x_3 = 20$			

Following the procedure used for the preceding three scenarios, the RSM formulations for displacement and stress under the three different earthquakes are presented separately in Equations (21) to (26).

$$D_{4N}(x_1, x_2, x_3) = -26.11 + 0.15x_1 + 0.39x_2 + 0.11x_3 \tag{21}$$

$$S_{4N}(x_1, x_2, x_3) = 1063.95 - 9.49x_1 - 11.96x_2 + 5.29x_3 + 0.11x_1x_2 - 0.05x_2x_3 - 0.02{x_2}^2 \tag{22}$$

$$D_{4F}(x_1, x_2, x_3) = -23.94 + 0.20x_1 + 0.21x_2 + 0.24x_3 \tag{23}$$

$$S_{4F}(x_1, x_2, x_3) = 531.67 - 4.51x_1 - 6.25x_2 + 4.37x_3 + 0.04x_1x_2 - 0.06x_2x_3 \tag{24}$$

$$D_{4T}(x_1, x_2, x_3) = -52.39 + 0.45x_1 + 0.54x_2 + 0.11x_3 \tag{25}$$

$$S_{4T}(x_1, x_2, x_3) = 734.03 - 7.73x_1 - 6.40x_2 + 3.58x_3 + 0.03x_1x_2 - 0.02x_1x_3 + 0.01{x_1}^2 \tag{26}$$

The results obtained from analysis of the findings for the four scenarios are evaluated and discussed in the following section.

5. Results and Discussion

In this section, the allowable failure limits for stress and displacement were first calculated from the mean values obtained from the analyses of the four scenarios. The reliability index and probability of failure were then estimated separately for each scenario. Failure occurs when the displacement (D) or stress (S) developed in the dam body exceeds the allowable displacement ($D_{(a)}$) or allowable stress ($S_{(a)}$), respectively. If either condition occurs, the structure is considered to have failed. According to the Incremental dynamic analyses (IDA) [21], the failure limit is defined at 84% of the range of structural-response variation. The difference is that in IDA, the response values are normally distributed random functions, whereas in the RSM they take a nonlinear polynomial form. This limit is therefore calculated according to Equation (27).

$$\Gamma_\mu = \left[\xi * \left(Max_\mu - Min_\mu\right)\right] + Min_\mu \tag{27}$$

where Γ_μ denotes the minimum or maximum limit of parameter μ, which represents displacement and stress. In addition, ξ denotes the failure level, which is defined as 84% (0.84) of the range of each variable. The maximum (Max_μ) and minimum (Min_μ) values of the parameter under consideration must be subtracted to calculate this range. Figure 18 to 23 give the calculation of the allowable values $D_{(1E_a)}$ and $S_{(1E_a)}$ for Scenario I.

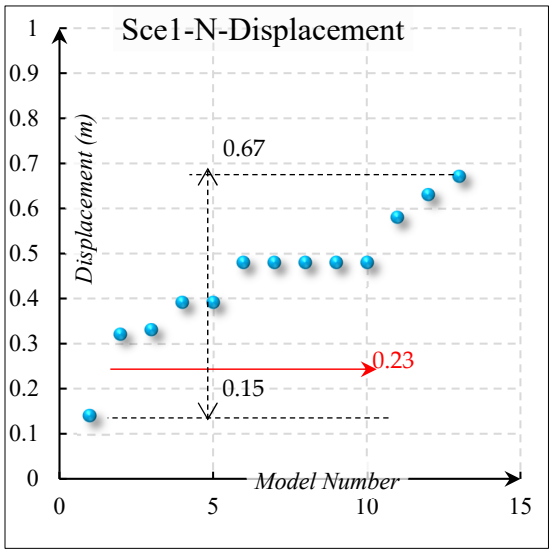


Figure 18. Displacement range in the first scenario under the Northridge earthquake.

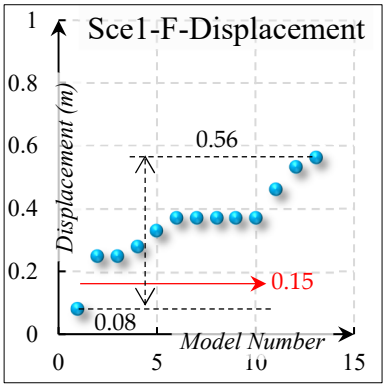


Figure 19. Displacement range in the first scenario under the Friuli earthquake.

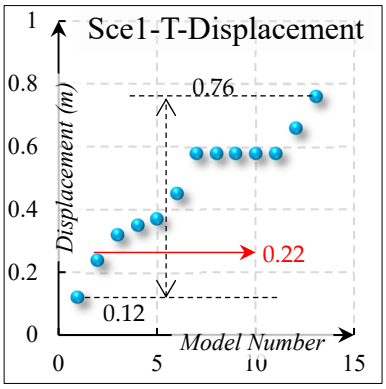


Figure 20. Displacement range in the first scenario under the Trinidad earthquake.

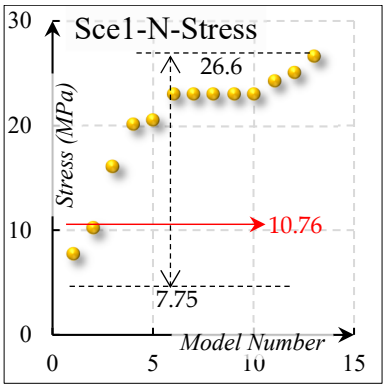


Figure 21. Stress range in the first scenario under the Northridge earthquake.

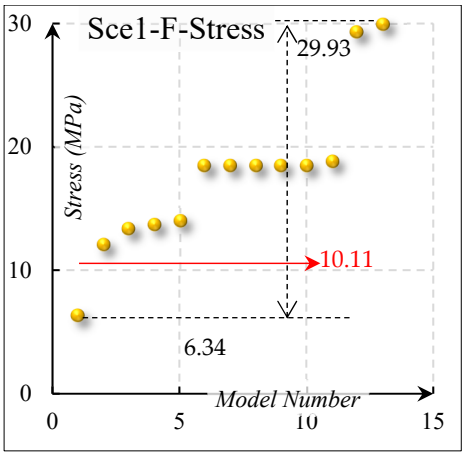


Figure 22. Stress range in the first scenario under the Friuli earthquake.

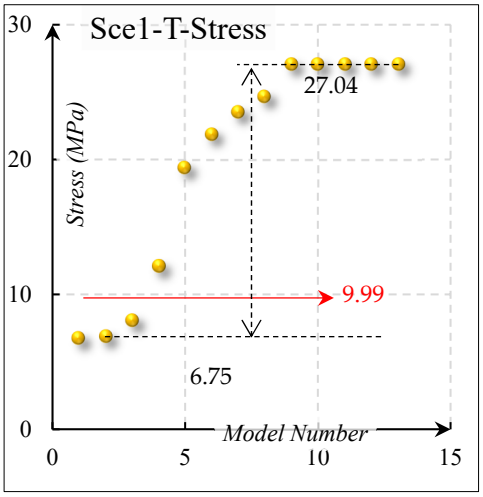


Figure 23. Stress range in the first scenario under the Trinidad earthquake.

As shown in the above figures, displacement and stress were sorted in ascending order. Structural safety was defined as the condition in which displacement and stress did not exceed 16% (100–86%) of the range, while 84% of the occurrence range was treated as the failure level. This process was repeated for all structures under the three different earthquakes. The mean displacement and stress obtained in the different cases at the 84% level were 0.191625 m and 10.57 MPa, respectively. The limit-state function g is therefore given by Equation (28).

$$g = \begin{pmatrix} D - D_{(a)} < 0 \\ S - S_{(a)} < 0 \end{pmatrix}, \qquad in\ wich:\ D_{(a)} = 0.191625\ m,\ S_{(a)} = 10.572\ MPa \tag{28}$$

where D and S are the displacement and stress developed in the structure, respectively, and are estimated from the relationships derived for each case. In addition, $D_{(a)}$ and $S_{(a)}$ are the allowable displacement and allowable stress, respectively. Reliability calculations for each case are performed below using this procedure.

5.1. Results of Scenario I: Asymmetric V-Shaped Valley

The reliability-analysis results for the relationships developed by the RSM for the asymmetric V-shaped valley in the first scenario are presented in Table 13. To obtain an accurate representation of the problem, all MCS analyses in this study were performed using 50 million random samples, and the analysis time for 50 million samples was less than 6 min in every case. The mean of each variable was set equal to the midpoint of its range, and the standard deviation was taken as 0.05 of the variable range in the original space. The problem space was ultimately transformed to the standard normal distribution with a mean of 0 and a standard deviation of 1, and the reliability calculations were performed in standard normal space.

Table 13. Reliability-analysis results for the models in the first scenario.

	Northridge			**Friuli**			**Trinidad**		
	MCS	**FORM**	**SORM**	**MCS**	**FORM**	**SORM**	**MCS**	**FORM**	**SORM**
P_f	10^{-5}	6×10^{-6}	9×10^{-6}	10^{-7}	9×10^{-8}	2×10^{-7}	4×10^{-5}	10^{-5}	4×10^{-5}
β	4.14	4.38	4.29	5.11	5.21	5.11	3.94	4.23	3.95

The mean reliability indices obtained from the three methods were 4.27 for the Northridge earthquake, 5.14 for the Friuli earthquake, and 4.04 for the Trinidad earthquake. It can therefore be concluded that the Friuli earthquake caused less failure in the structure. Meanwhile, the greatest damage to the dam body in V-shaped valleys occurred under the Trinidad earthquake. The overall mean reliability index in this case was 4.48, corresponding to a probability of failure of 3.8×10^{-6}.

Another important point evident from the above table is that the probability of failure obtained by FORM is lower than those obtained by the other two methods under all three earthquakes. This result suggests complexity and nonlinearity in the limit-state function. The concavity of the limit-state function in all three problems is represented in Figure 24. The figure provides a simplified illustration of the calculation of failure probability by the three methods.

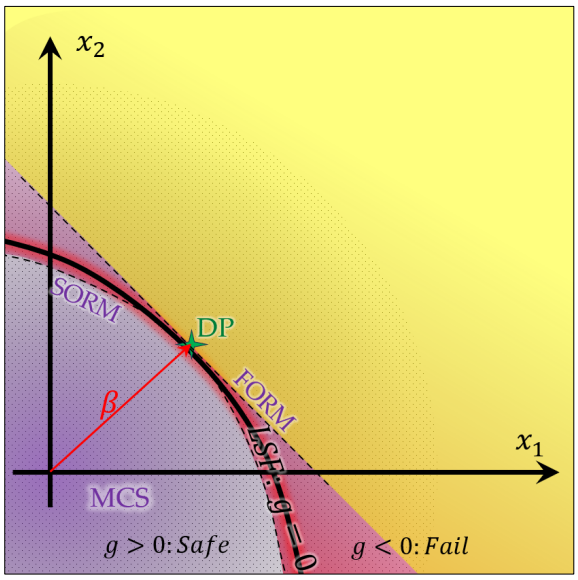


Figure 24. Approximation of the probability of failure by MCS, FORM, and SORM in Scenario I.

Figure 25 illustrates the indices obtained by the three methods under the three earthquakes, together with their means. The higher index obtained by FORM is also demonstrated in this figure. According to [21], the minimum index for structures of very high importance, such as concrete arch dams whose failure entails very high human and financial costs, is defined as 4.3. Figure 25 shows that the mean reliability index in this case exceeded 4.48. The high reliability index of the dam in this case can be attributed to the simple valley shape and the resulting high strength of the overall structural system.

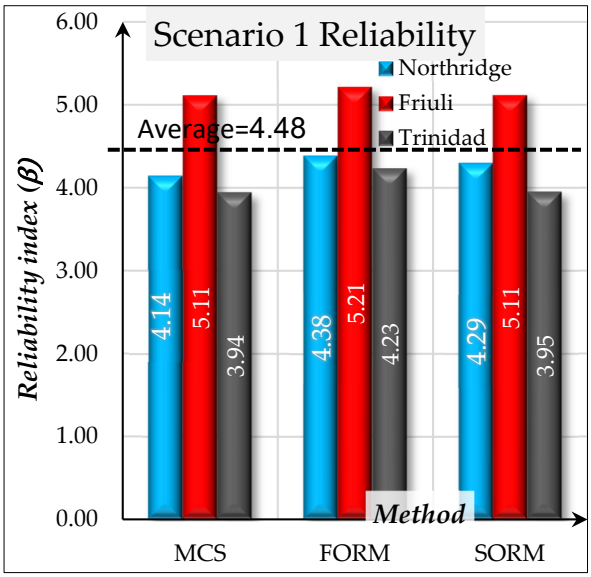


Figure 25. Reliability index in Scenario I.

5.2. Results of Scenario II: Symmetric Polygonal Valley

The limit-state function (g) was analyzed and evaluated separately, as in the preceding section, for the three earthquake records in the second scenario involving a symmetric polygonal valley. The numerical results are presented in Table 14, and their visual representation is provided in Figure 26.

Table 14. Reliability-analysis results for the models in the second scenario.

	Northridge			Friuli			Trinidad		
	MCS	**FORM**	**SORM**	**MCS**	**FORM**	**SORM**	**MCS**	**FORM**	**SORM**
P_f	4×10^{-5}	3×10^{-6}	10^{-4}	3×10^{-5}	9×10^{-7}	4×10^{-6}	10^{-5}	4×10^{-7}	10^{-6}
β	3.89	4.51	3.64	3.96	4.77	4.43	4.14	4.92	4.64

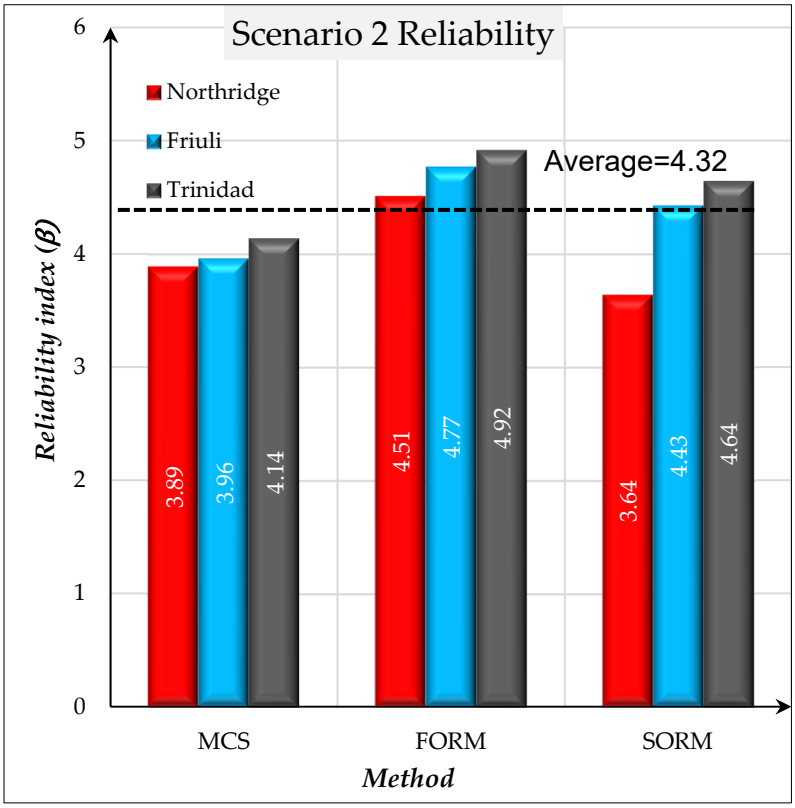


Figure 26. Reliability index in second Scenario.

Closer examination of the dam-system reliability results again shows that the index obtained by FORM is greater than those obtained by the other two methods for all three earthquakes. The concavity of the limit-state function is therefore the same as in Scenario I. The mean of the indices obtained by the three methods under the three earthquakes was again 4.32. In this scenario, the symmetry of the valley shape also provided suitable abutments for the dam body, and structural safety under earthquake loading satisfied the allowable code limit ($\beta_{dam} > 4.3$). All three methods also showed an overall similar trend in the response of the dam body to the three earthquakes. The Northridge earthquake caused the greatest failure in the structure in this case and was associated with the highest probability of failure. The Trinidad earthquake caused the least failure in the dam body.

5.3. Results of Scenario III: Asymmetric Polygonal Valley

The reliability-analysis results for the asymmetric polygonal valley in this scenario are presented numerically in Table 15 in terms of the reliability index and probability of failure and as bar charts in Figure 27.

Table 15. Reliability-analysis results for the models in the third scenario.

	Northridge			**Friuli**			**Trinidad**		
	MCS	**FORM**	**SORM**	**MCS**	**FORM**	**SORM**	**MCS**	**FORM**	**SORM**
P_f	3×10^{-5}	6×10^{-7}	10^{-5}	10^{-4}	8×10^{-5}	9×10^{-5}	10^{-4}	8×10^{-5}	10^{-4}
β	3.97	4.85	4.11	3.69	3.76	3.74	3.62	3.76	3.60

The calculated results for this scenario again show that the probabilities of failure obtained by FORM under all three earthquakes are lower than those obtained by MCS and SORM. These results suggest a concavity of the limit-state function similar to those in the first and second scenarios. For this valley shape, the Northridge earthquake caused the least failure in the structure, whereas the greatest effects of failure were observed under the Trinidad earthquake. This finding reflects the considerable complexity of seismic analyses and further emphasizes the need to use different seismic records when analyzing sensitive structures such as arch dams so that all possible events are evaluated. The seismic-reliability results for the arch dam in U-shaped valleys under the fourth scenario are presented and evaluated below.

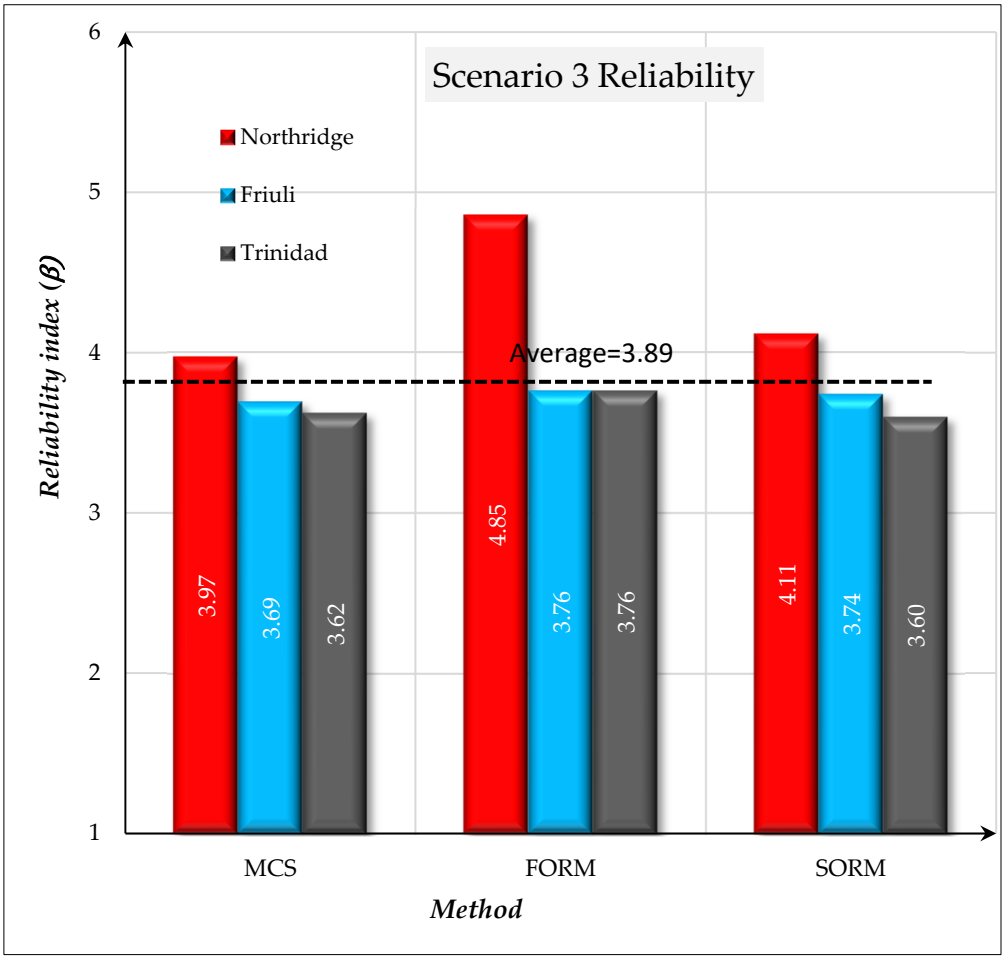


Figure 27. Reliability index in third Scenario.

5.4. Results of Scenario IV: U-Shaped Valley

Table 16 presents the reliability-analysis results for the problem, including the probability of failure (P_f) and reliability index (β) obtained using MCS, FORM, and SORM under the Northridge, Friuli, and Trinidad earthquakes for the symmetric U-shaped valley in the fourth scenario. It is of note that because of the low probability of failure in the problem, 50 million samples were used in the MCS method to provide adequate coverage of the sample space.

Table 16. Reliability-analysis results for the models in the fourth scenario.

	Northridge			Friuli			Trinidad		
	MCS	**FORM**	**SORM**	**MCS**	**FORM**	**SORM**	**MCS**	**FORM**	**SORM**
P_f	6×10^{-6}	4×10^{-6}	10^{-6}	8×10^{-6}	2×10^{-5}	8×10^{-6}	9×10^{-6}	10^{-5}	9×10^{-6}
β	4.83	4.42	4.69	4.29	4.02	4.31	4.28	4.23	4.27

Table 16 shows that the probability of failure obtained by FORM under all three earthquakes is higher than those obtained by Monte Carlo and SORM. It can therefore be concluded that the limit-state function has a concavity opposite to that of the preceding functions Figure 28. The shape of the limit-state function is emphasized because identifying its form is essential for accurate reliability analyses of different problems, selecting the most appropriate method, and obtaining the best result. The probability of failure produced by the Northridge earthquake was also lower than those produced by the other two earthquakes in all three methods (Figure 29).

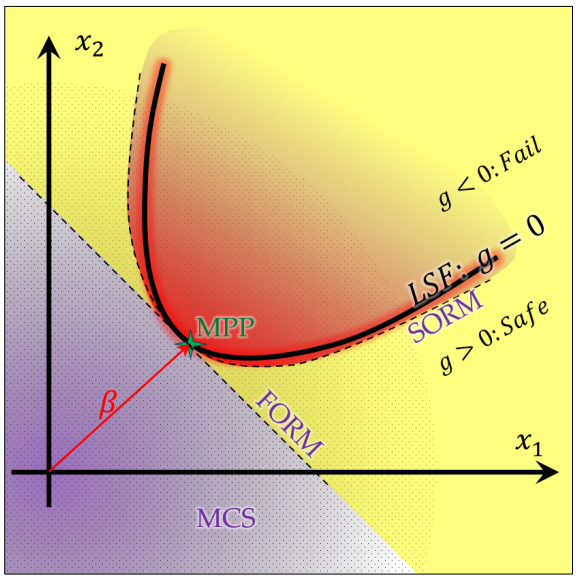


Figure 28. Approximation of the probability of failure by MCS, FORM, and SORM in Scenario IV.

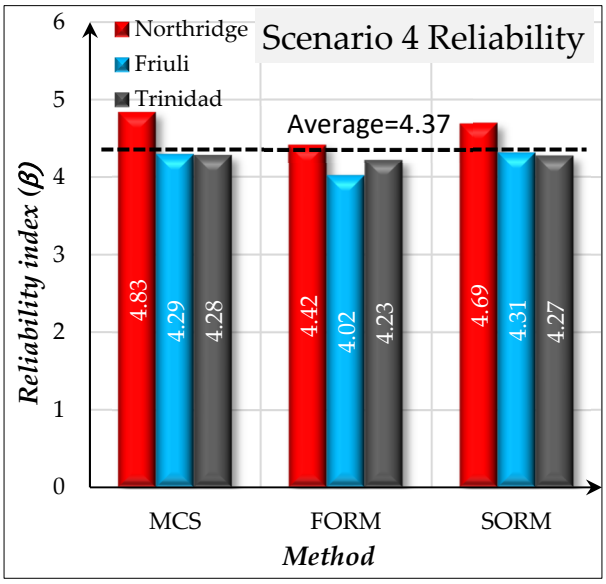


Figure 29. Reliability index in Scenario IV.

The overall findings of the present study are discussed in the following section.

6. Conclusions

Prediction of concrete strength in concrete structures is one of the most important challenges. This study comprehensively investigated the seismic reliability of concrete arch dams considering the effects of different valley shapes and seismic uncertainties. The results revealed that valley geometry, as a key factor in the seismic behavior of a dam, has a decisive role in stress transfer, the pattern of stress concentration in the arches, and the functional efficiency of the structure. The probabilistic assessment indicates that small changes in valley shape, in the presence of seismic uncertainties such as PGA intensity and earthquake frequency content, can produce substantial variation in the reliability index. These results further demonstrate the importance of probabilistic analyses based on diverse seismic data in the design of arch dams. The investigations showed that valley-shape symmetry directly increases the safety level of arch dams. This symmetry is associated with a more uniform stress distribution in the dam body and supports, thereby reducing the likelihood of damaging stress concentrations. In contrast, valleys with pronounced asymmetry increase the system's sensitivity to seismic uncertainties and exhibit a wider range of structural responses under different earthquake scenarios. This asymmetry increases the probability that responses will exceed allowable performance limits and emphasizes the need for more accurate analyses. The results also indicate that dams constructed in U-shaped valleys have, on average, the highest seismic

reliability index. This result is attributed to the appropriate support provided to the dam body by the abutments, favorable geometric stability, and reduced unwanted stress concentrations in the dam body. The reliability index obtained for this case fully satisfied the minimum code-recommended value ($\beta = 4.3$), indicating the high efficiency of this geometric arrangement under seismic uncertainty. Meanwhile, valleys with asymmetric sections reached a mean index of $\beta = 3.89$, which is below the allowable value and requires particular attention in seismic design and analysis so that acceptable code limits can be achieved. Overall, the findings of this study emphasize that, in the design of concrete arch dams, uncertainties associated with the actual valley shape must be considered carefully alongside earthquake characteristics. In this respect, selecting an appropriate valley geometry can contribute substantially to ensuring favorable seismic performance, increasing reliability, and achieving the safety level expected by codes. To ensure a minimum reliability index for new dam projects situated in asymmetric polygonal valley, the resulting dam geometry may require a high volume of concrete. Therefore, in such valley configurations, it is essential to optimize the dam's shape and incorporate fillets and haunch at the dam body abutments; this approach helps prevent fictious stress concentrations and reduces peak tensile and compressive stresses.

Author Contributions

M.A.: modelling, Formal analysis, Software, Writing—Original Draft; M.P.: Investigation, Methodology, modelling, Conceptualization, Supervision, Review & editing; S.P.: Investigation, data analysis, Data curation, Conceptualization, Supervision, Review & editing; All authors have read and agreed to the published version of the manuscript.

Funding

This research received no external funding.

Institutional Review Board Statement

Not applicable.

Informed Consent Statement

Not applicable.

Data Availability Statement

The data supporting the conclusions of this article will be made available by the authors on request.

Conflicts of Interest

The authors declare no conflict of interest.

Use of AI and AI-Assisted Technologies

No AI tools were utilized for this paper.

References

1. Fengjie, T.; Lahmer, T. Shape optimization based design of arch-type dams under uncertainties. *Eng. Optim.* **2018**, *50*, 1470–1482. https://doi.org/10.1080/0305215x.2017.1409348.
2. Nikkhakian, B.; Alembagheri, M.; Shayan, R.S. Parametric Investigation of Canyon Shape Effects on the Seismic Response of 3D Concrete Gravity Dam Model. *Geotech. Geol. Eng.* **2020**, *38*, 6755–6771. https://doi.org/10.1007/s10706-020-01467-3.
3. Zhang, M.Z.; Qiu, Y.X.; Xu, W.C.; et al. Effect of valley topography on dynamic response of arch dams. *Soil Dyn. Earthq. Eng.* **2024**, *186*, 108936. https://doi.org/10.1016/j.soildyn.2024.108936.
4. Pouraminian, M.; Ekranejad, H. Reliability analysis of concrete arch dam under stage construction and hydrostatic pressure by MCS and RS methods. *Sharif J. Civ. Eng.* **2021**, *37.2*, 135–145. https://doi.org/10.24200/j30.2021.56917.2871.
5. Pouraminian, M.; Pourbakhshian, S.; Farsangi, E.N.; et al. Probabilistic Safety Evaluation of a Concrete arch dam Based on Finite Element Modeling and A Reliability L-R Approach. *Civ. Environ. Eng. Rep.* **2019**, *29*, 62–78. https://doi.org/10.2478/ceer-2019-0044.

6. Pouraminian, M.; Pourbakhshian, S.; Noroozinejad Farsangi, E. Reliability Assessment and Sensitivity Analysis of Concrete Gravity Dams by Considering Uncertainty in Reservoir Water Levels and Dam Body Materials. *Civ. Environ. Eng. Rep.* **2020**, *30*, 1–17. https://doi.org/10.2478/ceer-2020-0001.
7. Pouraminian, M.; Pourbakhshian, S. Shape Optimization of Concrete Arch Dams with SPSA Algorithm and Post-Analysis of Pareto Front for Selection the Best Alternatives. *J. Hydraul. Struct.* **2020**, *6*, 59–82. https://doi.org/10.22055/jhs.2020.33293.1137.
8. Sun, B.; Deng, M.; Xu, J.; et al. Improved seismic performance assessment of high ACCWD based on the integrated seismic performance index and cloud—multiple stripes analysis method. *Soil Dyn. Earthq. Eng.* **2026**, *203*, 110093. https://doi.org/10.1016/j.soildyn.2026.110093.
9. Chen, Y.; Li, M.; Ren, Q.; et al. Efficiency-aware seismic fragility analysis of super-high arch dam using unsupervised ground motion clustering with probabilistic representation. *Adv. Eng. Informatics* **2026**, *71*, 104318. https://doi.org/10.1016/j.aei.2026.104318.
10. Xu, S.; Liu, J.; Yin, X.; et al. Seismic performance analysis of concrete dams considering the coupled effects of wavelet asymmetry and incident direction under near-fault ground motions. *Eng. Struct.* **2025**, *327*, 119670. https://doi.org/10.1016/j.engstruct.2025.119670.
11. Wu, Y.; Kang, F.; Chen, J.; et al. A hybrid data-mechanism-driven cloud model for spatiotemporal deformation-informed safety assessment of high arch dams. *Eng. Struct.* **2025**, *343*, 121019. https://doi.org/10.1016/j.engstruct.2025.121019.
12. Hasofer, A.M.; Lind, N.C. Exact and Invariant Second-Moment Code Format. *J. Eng. Mech. Div.* **1974**, *100*, 111–121. https://doi.org/10.1061/jmcea3.0001848.
13. Fiessler, B.; Neumann, H.J.; Rackwitz, R. Quadratic Limit States in Structural Reliability. *J. Eng. Mech. Div.* **1979**, *105*, 661–676. https://doi.org/10.1061/jmcea3.0002512.
14. Metropolis, N.; Ulam, S. The Monte Carlo Method. *J. Am. Stat. Assoc.* **1949**, *44*, 335–341. https://doi.org/10.1080/01621459.1949.10483310.
15. Mahab Ghods consulting engineer. *Final Report of Engineering Geology*; Mahab Ghods: Tehran, Iran, 2009. (In Farsi)
16. Mirzaei, E.; Vahdani, S.; Mirghaderi, R. Seismic analysis of double curved arch dams based performance. *World Congr. Eng. Comput. Sci.* **2010**, *1*, 1185.
17. Boggs, H.L. *Guide for Preliminary Design of Arch Dams*; Bureau of Reclamation: Denver, CO, USA, 1977.
18. Ghafari, S.; Aziz, H.A.; Isa, M.H.; et al. Application of response surface methodology (RSM) to optimize coagulation–flocculation treatment of leachate using poly-aluminum chloride (PAC) and alum. *J. Hazard. Mater.* **2009**, *163*, 650–656. https://doi.org/10.1016/j.jhazmat.2008.07.090.
19. Ghanbari Soumeh, K.; Parvini Sani, H. Optimization of through-bolt steel beam connection to CFST column reinforced with rib plates using RSM method and MCEO algorithm. *Numer. Methods Civ. Eng.* **2021**, *6*, 66–76. https://doi.org/10.52547/nmce.6.2.66.
20. Al-Shadeedi, M.B.; Hamdi, E.J. Comparison of the Structural Stability of Gravity Concrete Dams Using USACE and USBR Standards. *ARPN J. Eng. Appl. Sci. 2017, ISSN 1819-6608, 12, 1580–1592.*
21. Khorami, M.; Alvansazyazdi, M.; Shariati, M.; et al. Seismic performance evaluation of buckling restrained braced frames (BRBF) using incremental nonlinear dynamic analysis method (IDA). *Earthquakes Struct.* **2017**, *13*, 531–538. https://doi.org/10.12989/eas.2017.13.6.531.